Aerospace Science and Technology 155 (2024) 109694

Contents lists available at ScienceDirect

Aerospace Science and Technology

journal homepage: www.elsevier.com/locate/aescte

Enhancing the efficiency and energy capacity of the tri-directional FG nanoplate attached to the piezoelectric patch validated by artificial intelligence

Wenqing Yang [a], Lei Chang [a,*], Khalid A. Alnowibet [b], Mohammed El-Meligy [c,d]

[a] School of Carbon Neutrality Science and Technology, Anhui University of Science and Technology, Huainan, 232001, China
[b] Statistics and Operations Research Department, College of Science, King Saud University, Riyadh, 11451, Kingdom of Saudi Arabia
[c] Jadara University Research Center, Jadara University, Jordan
[d] Applied Science Research Center, Applied Science Private University, Amman, Jordan

ARTICLE INFO

Communicated by Jang-Kyo KIM

Keywords:
Wave propagation
Energy capacity
Artificial intelligence
Functionally graded material
Piezoelectric sensor and actuator
Optimization

ABSTRACT

Enhancing the efficiency and energy capacity in composite nanoelectromechanical systems (NEMS) holds significant importance in the engineering industry due to its critical role in enhancing the performance, reliability, and safety of aerospace structures and systems. One key area of application is in the development of advanced sensors and actuators. Regarding this issue, in the current work, enhancing the efficiency and energy capacity in the sandwich nanoplate with a tri-directional functionally graded layer and a piezoelectric patch layer is presented. For capturing the size effects, nonlocal strain-stress gradient theory with two size-dependent factors has been presented. The transverse shear deformation factor has an important role in the prediction of the mechanical performance of various structures. So, in the current work, a new four-variable refined quasi-3D logarithmic shear deformation theory has been investigated. Also, for cupling the piezoelectric patch and composite structure, compatibility conditions have been presented. Hamilton's principle with three factors has been presented for obtaining the coupled governing equations of the NEMS. For solving the current electrical system's partial differential equations, an analytical solution procedure has been presented. Also, to have a better understanding of the current electrical system's fundamental frequency, COMSOL tri-physics simulation has been presented. For verification of the results, one of the tools of artificial intelligence via the datasets of the mathematics and COMSOL multi-physics simulations is presented to verify the results for other input data with low computational cost. Finally, the effects of various factors such as the geometry of the piezoelectric patch, FG power index, length scale factor, nonlocal parameter, and location of the piezoelectric patch on the phase velocity have been discussed in detail. One of the important outcomes of the current work is that designers for modeling the NEMS should pay attention to the applied voltage, location, and geometry of the piezoelectric patch.

1. Introduction

The aerospace sector places great attention on wave propagation in NEMS because it plays a crucial role in improving the safety, dependability, and performance of aerospace systems and structures. The creation of sophisticated sensors and actuators is one important application area. With the use of wave propagation principles, NEMS-based sensors are able to precisely measure even the smallest variations in environmental factors like stress, pressure, and temperature. This skill is necessary to keep an eye on the structural integrity of aeronautical parts, guarantee early identification of any problems, and avert catastrophic failures. Another important aspect is the impact on communication systems. Wave propagation in NEMS can be harnessed to develop high-frequency communication devices that are crucial for maintaining reliable communication links in aerospace operations. The miniaturization enabled by NEMS technology allows for the integration of these communication devices into smaller, lighter, and more efficient systems, which is particularly advantageous for space missions where weight and space constraints are critical. In addition, wave propagation in NEMS contributes to the advancement of material science within the aerospace

* Corresponding author:
E-mail address: chang06@aust.edu.cn (L. Chang).

https://doi.org/10.1016/j.ast.2024.109694
Received 9 July 2024; Received in revised form 11 October 2024; Accepted 22 October 2024
Available online 28 October 2024

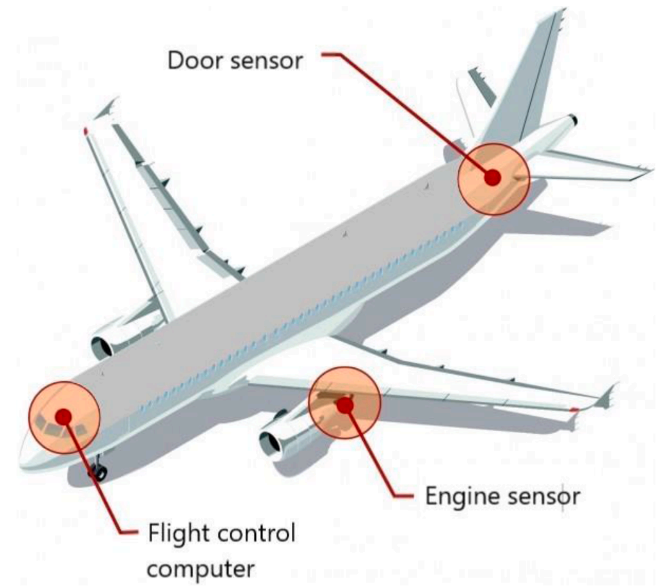

Fig. 1. One use of the FG nanoplate connected with a piezoelectric patch that was proposed as a sensor/actuator device for aircraft.

sector. By studying how waves propagate through different materials at the nanoscale, researchers can design and engineer materials with enhanced mechanical properties, such as increased strength, flexibility, and resistance to extreme conditions. These improved materials can lead to the development of more resilient and durable aerospace structures, capable of withstanding the harsh environments encountered during space travel. Furthermore, NEMS technology leveraging wave propagation can improve the precision and efficiency of navigation and control systems in aerospace vehicles. For instance, the accurate measurement of vibrations and dynamic responses in aircraft and spacecraft can lead to better control algorithms, resulting in smoother and more efficient flight dynamics. Overall, the importance of wave propagation in NEMS within the aerospace industry cannot be overstated. It enables the development of innovative solutions that enhance the safety, performance, and reliability of aerospace systems, paving the way for future advancements in the field. Fig. 1 illustrates one use of the FG nanoplate connected with a piezoelectric patch that was proposed as a sensor/actuator device for aircraft.

The analysis of the MEMS structure due to the non-locality and length-scale effects in small scales becomes challenging. In this regard, Controlling the buckling and vibrational stabilities in the micro-scale structures is an obstacle in using the devices made from FG materials and MEMS/NEMS [1,2]. Using piezoelectric patches on the micro-plates is one of the applicable methods to control the buckling and dynamical instability of the materials [3]. The governing equations of the FG materials usually involve non-linear terms. Further, the proper modeling of the plates and shells forces the researcher to employ shear deformation theories. Thus, both mathematical modeling and numerical solution approaches require formidable endeavor [4]. In this regard, several modeling approaches and solution methods can be found in the literature [5,6]. Safarpour et al. [7] employed NSGT to explore wave propagation in composite cylindrical nanoshells under thermal conditions. Hamilton's principle is employed to derive the governing equations and an analytical solution is provided. Higher-order shear deformation theory is used to model the nanoplates on an elastic substrate through NSGT by Ebrahimi and Dabbagh [8]. They also presented an analytical procedure to solve the governing equations. The importance of the length scale parameter is shown by Li et al [9] for functionally graded nano-beams. The buckling and vibrational characteristics of the beams were assessed via a generalized differential quadrature approach. There can be found several researches incorporating nonlocal theories in the analysis of nanoplates [10-12]. Piezoelectric patches to limit the vibrational instability of the micro/nano structures have been extensively investigated. Mahinzare et al. [13] investigated the applied voltage to piezoelectric layers on a rotating circular plate. It is demonstrated that the applied voltage significantly influences the natural frequency of the nano-plates. The effect of constant voltage on piezoelectric patches, which were used as actuators or sensors, was reported by Kargarnovin et al. [14]. The superior control of vibrations of the plates was acquired by increasing the feedback gain. This intensification in gain results in a decrease in displacement and frequency of the plates. The optimal positioning of piezoelectric patches on vibrating beams was considered by Bruant and Proslier [15]. They utilized optimization techniques to find the optimum location of the patches under different boundary conditions. Motlagh et al. [16] studied the effects of stiffness and mass contribution of the piezoelectric patches on the vibration modes and harmonic behavior of the functionally graded panels. It is observed in the reviewed literature that the piezoelectric patches both aid the control of the FG structures and strengthen the sandwich structures [17].

A sandwich nanoplate consists of multiple layers, typically with a lightweight core material sandwiched between stiff outer layers, enhancing its structural efficiency [18]. This configuration provides high stiffness-to-weight and strength-to-weight ratios, making it ideal for advanced applications such as aerospace, marine, and nanotechnology [19]. Due to its layered construction, the sandwich nanoplate exhibits superior resistance to buckling, vibration, and external forces [20]. Additionally, its nano-scale dimensions allow for enhanced mechanical properties, including increased resilience, durability, and thermal resistance [21]. The versatility of material selection for the core and face sheets offers tailored mechanical and thermal performance to meet specific design requirements [22].

Stability analysis is a critical aspect of engineering design, ensuring that structures and systems maintain their integrity and functionality under various loads and environmental conditions [23]. It allows engineers to predict potential failure modes, such as buckling or collapse, which can occur when structures are subjected to loads beyond their critical thresholds [24]. This analysis is essential for optimizing structural designs to resist dynamic disturbances, ensuring that they return to equilibrium without experiencing excessive deformations or instabilities [25]. In civil engineering, stability analysis guarantees the safe performance of infrastructure like bridges, buildings, and towers, especially under extreme conditions [26]. Similarly, in aerospace and mechanical engineering, it ensures that components like wings, beams, and rotating systems avoid destabilizing phenomena such as aeroelastic flutter or vibration-induced failures [27]. For composite materials and advanced structural systems, stability analysis helps assess their behavior under complex loading scenarios, ensuring their reliability in demanding environments [28]. It also plays a pivotal role in the design of offshore and marine structures, where unpredictable environmental forces pose significant risks to stability [29]. By accurately determining the safe load-carrying capacities of structures, stability analysis aids in preventing catastrophic failures and extending the service life of engineering systems [30]. Additionally, it supports the optimization of material use, contributing to more efficient and cost-effective designs [31]. Ultimately, stability analysis enhances the safety, reliability, and durability of engineering designs, reducing the likelihood of unexpected failures and promoting long-term sustainability [32].

As a first attempt, in the current work, absorbed energy capacity, and wave dispersion characteristics of the NEMS coupled with the piezoelectric patch are presented. For capturing the size effects, nonlocal strain-stress gradient theory with two size-dependent factors is presented. The transverse shear deformation factor has an important role in the prediction of the mechanical performance of various structures. So, in the current work, a new four-variable refined quasi-3D logarithmic shear deformation theory is investigated. With the aid of Hamilton's principle and analytical solution procedure, the current electrical

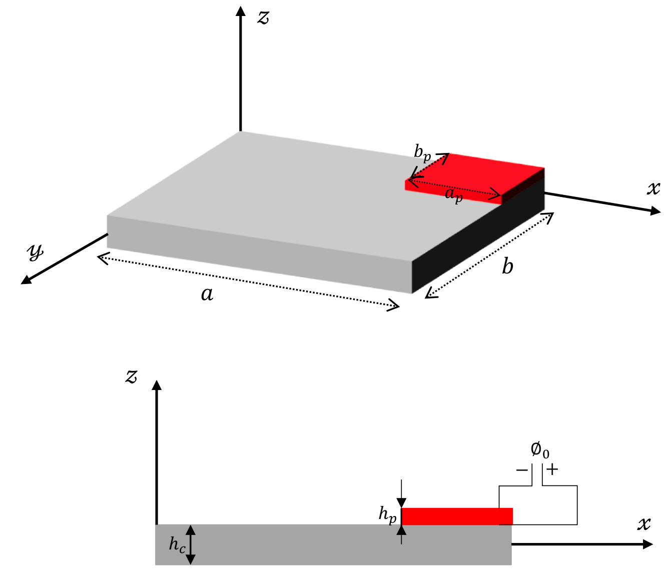

Fig. 2. Sandwich diagrammatic drawing NEMS.

system's partial differential equations are derived and solved, respectively. For a better understanding of the current electrical system's fundamental frequency, COMSOL multi-physics simulation has been presented. For verification of the results, one of the tools of artificial intelligence via the datasets of the mathematics and COMSOL multi-physics simulations is presented to verify the results for other input data with low computational cost. Finally, the effects of various factors such as the geometry of the piezoelectric patch, FG power index, length scale factor, nonlocal parameter, and location of the piezoelectric patch on the phase velocity have been discussed in detail.

2. Mathematical simulation

Analyze the sandwich nanostructure shown in Fig. 2 which has a patch piezoelectric face-sheet layer and a FGM core. The face-sheet layer has thicknesses of h_p, the core has thicknesses of h_c, the piezoelectric patch has lengths of a_p and b_p, the core has widths of a and b, the length of the core is a, and the initial external electric field is ϕ_0. The equations for the motion of waves are expected to be obtained in a system of Cartesian coordinates $(x,\ y,\ z)$.

2.1. Tri-directional functionally graded materials (TD-FGMs)

The modified power law defines the material property $(\mathbb{E}, \nu, \rho)$ of the TD-FGMs core layer as follows:

$$\mathbb{E}_c(x,y,z) = \mathbb{E}_m + (\mathbb{E}_c - \mathbb{E}_m)\left(\frac{x}{a}\right)^{n_x}\left(\frac{y}{b}\right)^{n_y}\left(0.5+\frac{z}{h}\right)^{n_z}. \tag{1a}$$

$$\nu_c(x,y,z) = \nu_m + (\nu_c - \nu_m)\left(\frac{x}{a}\right)^{n_x}\left(\frac{y}{b}\right)^{n_y}\left(0.5+\frac{z}{h}\right)^{n_z}. \tag{1b}$$

$$\rho_c(x,y,z) = \rho_m + (\rho_c - \rho_m)\left(\frac{x}{a}\right)^{n_x}\left(\frac{y}{b}\right)^{n_y}\left(0.5+\frac{z}{h}\right)^{n_z}. \tag{1c}$$

where the power law index is indicated in the x-, y-, and z- directions by the variables n_x, n_y, and n_z. Furthermore, the ceramic and metal phases are indicated by $()_c$ and $()_m$. Furthermore, the mass density of the core, Poisson's ratio, and Young's modulus are indicated by the values of $E(x,y,z)$, $\nu(x,y,z)$, and $\rho(x,y,z)$, respectively. It should be emphasized that for FGMs, the neutral plane is not in the midplane, despite the fact that we assume this in our work [33].

2.2. Mathematical modeling

2.2.1. The nonlocal strain gradient theory

The stiffness-hardening and softening-stiffness processes of nano-size structure systems have been found in the characteristics of nano-structures via experimental observations and molecular dynamic simulations [34]. The above-indicated processes may be considered using the nonlocal strain gradient elasticity, a non-classical continuum theory [34].

$$\sigma_{ij} - \mu^2\sigma_{ij,mm} = C_{ijkl}\left(\mathscr{E}_{kl} - l^2\mathscr{E}_{kl,mm}\right). \tag{2}$$

where the elastic moduli are characterized using C_{ijkl}; the stiffness-enhancement process is anticipated by the strain gradient parameter (l); the softening-stiffness mechanism is predicted by the nonlocal parameter (μ). The stress and strain tensors are indicated by σ_{ij} and $\mathscr{E}_{ij}$, respectively. Note: Strain gradient one [35] and Eringen's nonlocal elasticity model [36] may be obtained by adding the following forms to Eq. (2), where $l = 0$ or $\mu = 0$.

$$\begin{aligned}&(1-\mu^2\nabla^2)\sigma_{ij} = t_{ij},\\ &\sigma_{ij} = C_{ijkl}\left(\mathscr{E}_{ij} - l^2\mathscr{E}_{ij,mm}\right).\end{aligned} \tag{3}$$

in which the Laplacian operator is represented by $\nabla^2 = \frac{\partial^2}{\partial x^2} + \frac{\partial^2}{\partial y^2}$.

2.2.2. Displacement field

The new four-variable refined quasi-3D logarithmic shear deformation theory (RQ-3DLSDT), which accounts for thickness stretching, is described in this section. The following is a representation of the core displacement field [37]:

$$\begin{aligned}u_c(x,y,z,t) &= u_{0c}(x,y) - z\frac{\partial w_{0c}(x,y)}{\partial x} + f(z)\frac{\partial w_{1c}(x,y)}{\partial x},\\ v_c(x,y,z,t) &= v_{0c}(x,y) - z\frac{\partial w_{0c}(x,y)}{\partial y} + f(z)\frac{\partial w_{1c}(x,y,t)}{\partial y},\\ w_c(x,y,z,t) &= w_{0c}(x,y) + \mathscr{G}(z)w_{1c}(x,y).\end{aligned} \tag{4}$$

where u_c, v_c, and w_c denote the displacement components of a TD-FGMs core layer in the x, y, and z directions. As can be seen, there are only four unknown variables in the displacement field discussed earlier: $w_{1c}(x,y)$ is an extra displacement that is assumed to be a result of normal stress. The variables $u_{0c}(x,y)$, $v_{0c}(x,y)$ and $w_{0c}(x,y)$, respectively, indicate the displacements of the center plane ($z = 0$) in the x, y, and z directions. $f(z) = 3h\ln[(h-z)/(h+z)]/8 + 4z^3/3h^2$ and $\mathscr{G}(z) = -h^2/4\left(h^2 - z^2\right) + 4z^2/3h^2$, respectively, are the proposed transverse shear deformation functions. The displacement field of a patch piezoelectric is shown as follows [38]:

$$\begin{aligned}u_p(x,y,z,t) &= u_{0p}(x,y) + zu_{1p}(x,y),\\ v_p(x,y,z,t) &= v_{0p}(x,y) + zv_{1p}(x,y),\\ w_p(x,y,z,t) &= w_{0p}(x,y).\end{aligned} \tag{5}$$

where u_p, v_p, and w_p denote the displacement components of a patch piezoelectric in the x, y, and z directions. The variables $u_{0c}(x,y)$, $v_{0c}(x,y)$ and $w_{0c}(x,y)$, respectively, indicate the displacements of the center plane ($z = \frac{h_c}{2} + \frac{h_p}{2}$) in the x, y, and z directions. Also, whereas u_{1p} and v_{1p} indicate the mid-plane's rotations in the xz and yz planes, correspondingly [39].

2.2.3. Compatibility conditions

According to the compatibility relations, the following is true if perfect bonding conditions are present at the top and bottom face sheet-core interfaces [40]:

$$u_p\left(x,y,\frac{h_c}{2}\right)=u_c\left(x,y,\frac{h_c}{2}\right),$$
$$v_p\left(x,y,\frac{h_c}{2}\right)=v_c\left(x,y,\frac{h_c}{2}\right), \tag{6}$$
$$w_p\left(x,y,\frac{h_c}{2}\right)=w_c\left(x,y,\frac{h_c}{2}\right),$$

It may be written using Eqs. (4), (5), and (6) to represent displacement fields.

$$
\begin{aligned}
u_c(x,y,z,t)&=u_{0c}(x,y)-z\frac{\partial w_{0c}(x,y)}{\partial x}+f(z)\frac{\partial w_{1c}(x,y)}{\partial x},\\
v_c(x,y,z,t)&=v_{0c}(x,y)-z\frac{\partial w_{0c}(x,y)}{\partial y}+f(z)\frac{\partial w_{1c}(x,y)}{\partial y},\\
w_c(x,y,z,t)&=w_{0c}(x,y)+G(z)w_{1c}(x,y),\\
u_p(x,y,z,t)&=u_{0c}(x,y)-\frac{h_c}{2}\frac{\partial w_{0c}(x,y)}{\partial x}+f\left(\frac{h_c}{2}\right)\frac{\partial w_{1c}(x,y)}{\partial x}+\left(z-\frac{h_c}{2}\right)u_{1p}(x,y),\\
v_p(x,y,z,t)&=v_{0c}(x,y)-\frac{h_c}{2}\frac{\partial w_{0c}(x,y)}{\partial y}+f\left(\frac{h_c}{2}\right)\frac{\partial w_{1c}(x,y)}{\partial y}+\left(z-\frac{h_c}{2}\right)v_{1p}(x,y),\\
w_p(x,y,z,t)&=w_{0c}(x,y)+G\left(\frac{h_c}{2}\right)w_{1c}(x,y).
\end{aligned} \tag{7}
$$

If the following definition of strain displacement applies

$$
\begin{aligned}
&\varepsilon_{xx}=\frac{\partial u}{\partial x},\ \varepsilon_{yy}=\frac{\partial v}{\partial y},\ \varepsilon_{zz}=\frac{\partial w}{\partial z},\ \varepsilon_{xz}=\frac{\partial u}{\partial z}+\frac{\partial w}{\partial x},\\
&\varepsilon_{xy}=\frac{\partial u}{\partial y}+\frac{\partial v}{\partial x},\ \varepsilon_{yz}=\frac{\partial v}{\partial z}+\frac{\partial w}{\partial y}.
\end{aligned} \tag{8}
$$

The non-null strain components of the core and piezoelectric layer are then defined as:

$$
\begin{aligned}
\varepsilon_{xxc}&=\frac{\partial u_{0c}(x,y)}{\partial x}-z\frac{\partial^2 w_{0c}(x,y)}{\partial x^2}+f(z)\frac{\partial^2 w_{1c}(x,y)}{\partial x^2},\\
\varepsilon_{yyc}&=\frac{\partial v_{0c}(x,y)}{\partial y}-z\frac{\partial^2 w_{0c}(x,y)}{\partial y^2}+f(z)\frac{\partial^2 w_{1c}(x,y)}{\partial y^2},\\
\varepsilon_{zzc}&=G_1(z)w_{1c},\\
\varepsilon_{xzc}&=f_1(z)\frac{\partial w_{1c}}{\partial x}+G(z)\frac{\partial w_{1c}}{\partial x},\\
\varepsilon_{yzc}&=f_1(z)\frac{\partial w_{1c}}{\partial y}+G(z)\frac{\partial w_{1c}}{\partial y},\\
\varepsilon_{xyc}&=\left(\frac{\partial u_{0c}(x,y)}{\partial y}+\frac{\partial v_{0c}(x,y)}{\partial x}\right)-2z\frac{\partial^2 w_{0c}(x,y)}{\partial x\partial y}+2f(z)\frac{\partial^2 w_{1c}(x,y)}{\partial x\partial y},\\
\varepsilon_{xxp}&=\frac{\partial u_{0c}(x,y)}{\partial x}-\frac{h_c}{2}\frac{\partial^2 w_{0c}(x,y)}{\partial x^2}+f\left(\frac{h_c}{2}\right)\frac{\partial^2 w_{1c}(x,y)}{\partial x^2}+\left(z-\frac{h_c}{2}\right)\frac{\partial u_{1p}(x,y)}{\partial x},\\
\varepsilon_{yyp}&=\frac{\partial v_{0c}(x,y)}{\partial y}-\frac{h_c}{2}\frac{\partial^2 w_{0c}(x,y)}{\partial y^2}+f\left(\frac{h_c}{2}\right)\frac{\partial^2 w_{1c}(x,y)}{\partial y^2}+\left(z-\frac{h_c}{2}\right)\frac{\partial v_{1p}(x,y)}{\partial y},\\
\varepsilon_{zzp}&=0,\\
\varepsilon_{xzp}&=u_{1p}+\frac{\partial w_{0c}}{\partial x}+G\left(\frac{h_c}{2}\right)\frac{\partial w_{1c}}{\partial x},\\
\varepsilon_{yzp}&=v_{1p}+\frac{\partial w_{0c}}{\partial y}+G\left(\frac{h_c}{2}\right)\frac{\partial w_{1c}}{\partial y},
\end{aligned} \tag{9}
$$

$$
\begin{aligned}
\varepsilon_{xyp}=&\left(\frac{\partial u_{0c}(x,y)}{\partial y}+\frac{\partial v_{0c}(x,y)}{\partial x}\right)-h_c\frac{\partial^2 w_{0c}(x,y)}{\partial x\partial y}+2f\left(\frac{h_c}{2}\right)\frac{\partial^2 w_{1c}(x,y)}{\partial x\partial y}\\
&+\left(z-\frac{h_c}{2}\right)\left(\frac{\partial u_{1p}(x,y)}{\partial y}+\frac{\partial v_{1p}(x,y)}{\partial x}\right).
\end{aligned}
$$

where $f_1(z)=\frac{\partial f(z)}{\partial z}$, and $G_1(z)=\frac{\partial G(z)}{\partial z}$.

It is possible to update the nonlocal strain gradient theory of the current theory to recast Eq. (2) as follows:

$$
\begin{aligned}
(1-\mu^2\nabla^2)\sigma_{xxc}&=(1-l^2\nabla^2)\left(Q_{11c}\varepsilon_{xxc}+Q_{12c}\varepsilon_{yyc}+Q_{13c}\varepsilon_{zzc}\right),\\
(1-\mu^2\nabla^2)\sigma_{yyc}&=(1-l^2\nabla^2)\left(Q_{12c}\varepsilon_{xxc}+Q_{22c}\varepsilon_{yyc}+Q_{23c}\varepsilon_{zzc}\right),\\
(1-\mu^2\nabla^2)\sigma_{zzc}&=(1-l^2\nabla^2)\left(Q_{13c}\varepsilon_{xxc}+Q_{23c}\varepsilon_{yyc}+Q_{33c}\varepsilon_{zzc}\right),\\
(1-\mu^2\nabla^2)\sigma_{yzc}&=(1-l^2\nabla^2)Q_{44c}\varepsilon_{yzc},\\
(1-\mu^2\nabla^2)\sigma_{xzc}&=(1-l^2\nabla^2)Q_{55c}\varepsilon_{xzc},\\
(1-\mu^2\nabla^2)\sigma_{xyc}&=(1-l^2\nabla^2)Q_{66c}\varepsilon_{xyc},
\end{aligned} \tag{10}
$$

where

$$
\begin{aligned}
&Q_{11c}=\frac{\mathbb{E}_c(x,y,z)(1-\nu_c(x,y,z))}{(1+\nu_c(x,y,z))(1-2\nu_c(x,y,z))},\ Q_{33c}=Q_{22c}=Q_{11c}\\
&Q_{12c}=\frac{\nu_c(x,y,z)\mathbb{E}_c(x,y,z)}{(1+\nu_c(x,y,z))(1-2\nu_c(x,y,z))},\ Q_{13c}=Q_{23c}=Q_{12c},\\
&Q_{44c}=\frac{\mathbb{E}_c(x,y,z)}{2(1+\nu_c(x,y,z))},\ Q_{66c}=Q_{55c}=Q_{44c}
\end{aligned} \tag{11}
$$

The constitutive relations for the piezoelectric layers are developed as:

$$
\begin{aligned}
(1-\mu^2\nabla^2)\sigma_{xxp}&=(1-l^2\nabla^2)\left(Q_{11p}\varepsilon_{xxp}+Q_{12p}\varepsilon_{yyp}-e_{31p}E_z\right),\\
(1-\mu^2\nabla^2)\sigma_{yyp}&=(1-l^2\nabla^2)\left(Q_{12p}\varepsilon_{xxp}+Q_{22p}\varepsilon_{yyp}-e_{32p}E_z\right),\\
(1-\mu^2\nabla^2)\sigma_{yzp}&=(1-l^2\nabla^2)\left(Q_{44p}\varepsilon_{yzp}-e_{24p}E_y\right),\\
(1-\mu^2\nabla^2)\sigma_{xzp}&=(1-l^2\nabla^2)\left(Q_{55p}\varepsilon_{xzp}-e_{15p}E_x\right),\\
(1-\mu^2\nabla^2)\sigma_{xyp}&=(1-l^2\nabla^2)\left(Q_{66p}\varepsilon_{xyp}\right),
\end{aligned} \tag{12}
$$

The electric displacement relations are developed as

$$
\begin{aligned}
(1-\mu^2\nabla^2)D_{xp}&=(1-l^2\nabla^2)\left(e_{15p}\varepsilon_{xzp}+T_{11p}E_x\right),\\
(1-\mu^2\nabla^2)D_{yp}&=(1-l^2\nabla^2)\left(e_{15p}\varepsilon_{yzp}+T_{22p}E_y\right),\\
(1-\mu^2\nabla^2)D_{zp}&=(1-l^2\nabla^2)\left(e_{31p}\varepsilon_{xxp}+e_{32p}\varepsilon_{yyp}+T_{33p}E_z\right),
\end{aligned} \tag{13}
$$

where

$$
\begin{aligned}
&Q_{11p}=Q_{11}-\frac{Q_{13}^2}{Q_{33}},\ Q_{12p}=Q_{12}-\frac{Q_{13}Q_{23}}{Q_{33}},\ Q_{22p}=Q_{22}-\frac{Q_{23}^2}{Q_{33}},\\
&Q_{44p}=Q_{44},Q_{55p}=Q_{55},Q_{66p}=Q_{66},\\
&e_{31p}=e_{31}-\frac{Q_{13}e_{33}}{Q_{33}},e_{32p}=e_{32}-\frac{Q_{23}e_{33}}{Q_{33}},e_{15p}=e_{15},e_{24p}=e_{24},\\
&T_{11p}=T_{11},T_{22p}=T_{22},T_{33p}=T_{33}+\frac{e_{33}^2}{Q_{33}},
\end{aligned} \tag{14}
$$

The equivalent electric field strengths, E_x, E_y, E_z, that are part of Eqs. (12) and (13), may be written as follows [1,2,41]:

$$E_x=-\frac{\partial\psi}{\partial x},E_y=-\frac{\partial\psi}{\partial y},E_z=-\frac{\partial\psi}{\partial z}, \tag{15}$$

The following explanation may be given for the electric potential $\psi(x,y,z,t)$:

$$\psi(x,y,z,t)=-\cos(\beta z)\phi(x,y,t)+\frac{2z\phi_0}{h}. \tag{16}$$

where $\beta=\pi/h$ and ϕ_0 represents the initial external electric field. Moreover, $\phi(x,y,t)$ defines a spatial variation for the electric potential in the x and y axes.

2.3. Hamilton's principle and governing equations

The following variational energy form is obtained by applying Hamilton's principle [40,42] to the fundamental equations of the problem.

$$\int_{t_1}^{t_2}(\delta\mathfrak{T}_k-(\delta\mathfrak{T}_e-\delta\mathfrak{T}_w))dt=0. \tag{17}$$

where $\mathfrak{I}_k$, $\mathfrak{I}_e$, and $\mathfrak{I}_w$ stand for the system's work done, strain energy, and kinetic energy, respectively. The quantities given above are explained in the following sentences.

$$\mathfrak{I}_k = \int \rho_b \left[\left(\frac{\partial u_c}{\partial t} \right)^2 + \left(\frac{\partial v_c}{\partial t} \right)^2 + \left(\frac{\partial w_c}{\partial t} \right)^2 \right] dV + \int \rho_p \left[\left(\frac{\partial u_p}{\partial t} \right)^2 + \left(\frac{\partial v_p}{\partial t} \right)^2 + \left(\frac{\partial w_p}{\partial t} \right)^2 \right] dV, \tag{18}$$

$$\mathfrak{I}_e = \int \{ \sigma_{xxc} \mathscr{E}_{xxc} + \sigma_{yyc} \mathscr{E}_{yyc} + \sigma_{zzc} \mathscr{E}_{zzc} + \sigma_{yzc} \mathscr{E}_{yzc} + \sigma_{xzc} \mathscr{E}_{xzc} + \sigma_{xyc} \mathscr{E}_{xyc} \} dV + \int \left\{ \begin{array}{c} \sigma_{xxp} \mathscr{E}_{xxp} + \sigma_{yyp} \mathscr{E}_{yyp} + \sigma_{zzp} \mathscr{E}_{zzp} + \sigma_{yzp} \mathscr{E}_{yzp} + \sigma_{xzp} \mathscr{E}_{xzp} \\ + \sigma_{xyp} \mathscr{E}_{xyp} - \mathscr{D}_{xp} E_{xp} - \mathscr{D}_{yp} E_{yp} - \mathscr{D}_{zp} E_{zp} \end{array} \right\} dV.$$

The first change in the amount of work done with respect to the external electric force applied is:

$$\mathfrak{I}_w = \frac{1}{2} \int \mathscr{N}_p \left[\left(\frac{\partial w_{0c}}{\partial x} \right)^2 + \left(\frac{\partial w_{0c}}{\partial y} \right)^2 \right] dA, \tag{19}$$

The following might be used to determine the electric load:

$$\mathscr{N}_P = -2 \left(e_{31} - \frac{\mathfrak{Q}_{13} e_{33}}{\mathfrak{Q}_{33}} \right) \phi_0. \tag{20}$$

Where ϕ_0 is the initial external electric potential. Eqs. (17) and (19) may be substituted into Eq. (16) along with a few mathematical procedures to provide the following equations.

$$\delta u_{0c}: \begin{array}{c} \frac{\partial \mathscr{N}_{xxc}}{\partial x} + \frac{\partial \mathscr{N}_{xyc}}{\partial y} + \frac{\partial \mathscr{N}_{xxp}}{\partial x} + \frac{\partial \mathscr{N}_{xyp}}{\partial y} = \mathscr{I}_{0c} \frac{\partial^2 u_{0c}}{\partial t^2} - \mathscr{I}_{1c} \frac{\partial^3 w_{0c}}{\partial x \partial t^2} + \mathscr{I}_{2c} \frac{\partial^3 w_{1c}}{\partial x \partial t^2} \\ + \mathscr{I}_{0p} \frac{\partial^2 u_{0c}}{\partial t^2} - \mathscr{I}_{1p} \frac{\partial^3 w_{0c}}{\partial x \partial t^2} + \mathscr{I}_{2p} \frac{\partial^3 w_{1c}}{\partial x \partial t^2} + \mathscr{I}_{3p} \frac{\partial^2 u_{1c}}{\partial t^2} \end{array}, \tag{21a}$$

$$\delta v_{0c}: \begin{array}{c} \frac{\partial \mathscr{N}_{yyc}}{\partial y} + \frac{\partial \mathscr{N}_{xyc}}{\partial x} + \frac{\partial \mathscr{N}_{yyp}}{\partial y} + \frac{\partial \mathscr{N}_{xyp}}{\partial x} = \mathscr{I}_{0c} \frac{\partial^2 v_{0c}}{\partial t^2} - \mathscr{I}_{1c} \frac{\partial^3 w_{0c}}{\partial y \partial t^2} + \mathscr{I}_{2c} \frac{\partial^3 w_{1c}}{\partial y \partial t^2} \\ + \mathscr{I}_{0p} \frac{\partial^2 v_{0c}}{\partial t^2} - \mathscr{I}_{1p} \frac{\partial^3 w_{0c}}{\partial y \partial t^2} + \mathscr{I}_{2py} \frac{\partial^3 w_{1c}}{\partial y \partial t^2} + \mathscr{I}_{3py} \frac{\partial^2 v_{1c}}{\partial t^2} \end{array}, \tag{21b}$$

$$\delta w_{0c}: \begin{array}{c} \frac{\partial^2 \mathscr{M}_{xxc}}{\partial x^2} + \frac{\partial^2 \mathscr{M}_{yyc}}{\partial y^2} + 2 \frac{\partial^2 \mathscr{M}_{xyc}}{\partial x \partial y} + \frac{\partial^2 \mathscr{M}_{xxp}}{\partial x^2} + \frac{\partial^2 \mathscr{M}_{yyp}}{\partial y^2} + 2 \frac{\partial^2 \mathscr{M}_{xyp}}{\partial x \partial y} + \frac{\partial \mathscr{N}_{xzp}}{\partial x} + \frac{\partial \mathscr{N}_{yzp}}{\partial y} \\ + 2 \frac{\partial^2 \mathscr{M}_{xyp}}{\partial x \partial y} - \mathscr{N}_P \left(\frac{\partial^2 w_{0c}}{\partial x^2} + \frac{\partial^2 w_{0c}}{\partial y^2} \right) = \mathscr{I}_{0c} \frac{\partial^2 w_{0c}}{\partial t^2} + \mathscr{I}_{1c} \frac{\partial^2 w_{1c}}{\partial t^2} + \mathscr{O}_{0p} \frac{\partial^2 w_p}{\partial t^2} \\ + \mathscr{O}_{1p} \frac{\partial^2 w_{1p}}{\partial t^2} - \frac{\partial}{\partial x} \left(\mathscr{L}_{0cx} \frac{\partial^2 u_{0c}}{\partial t^2} \right) + \frac{\partial}{\partial x} \left(\mathscr{L}_{1cx} \frac{\partial^3 w_{0c}}{\partial x \partial t^2} \right) - \frac{\partial}{\partial x} \left(\mathscr{L}_{2cx} \frac{\partial^3 w_{1c}}{\partial x \partial t^2} \right) \\ - \frac{\partial}{\partial y} \left(\mathscr{L}_{0c} \frac{\partial^2 v_{0c}}{\partial t^2} \right) + \frac{\partial}{\partial y} \left(\mathscr{L}_{1c} \frac{\partial^3 w_{0c}}{\partial y \partial t^2} \right) - \frac{\partial}{\partial y} \left(\mathscr{L}_{2c} \frac{\partial^3 w_{1c}}{\partial y \partial t^2} \right) - \mathscr{L}_{0p} \frac{\partial^3 u_{0c}}{\partial x \partial t^2} + \mathscr{L}_{1p} \frac{\partial^4 w_{0c}}{\partial x^2 \partial t^2} \\ - \mathscr{L}_{2p} \frac{\partial^4 w_{1c}}{\partial x^2 \partial t^2} - \mathscr{L}_{3p} \frac{\partial^2 u_{1p}}{\partial t^2} - \mathscr{L}_{0p} \frac{\partial^3 v_{0c}}{\partial x \partial t^2} + \mathscr{L}_{1p} \frac{\partial^4 w_{0c}}{\partial y^2 \partial t^2} - \mathscr{L}_{2p} \frac{\partial^4 w_{1c}}{\partial y^2 \partial t^2} - \mathscr{L}_{3p} \frac{\partial^2 v_{1p}}{\partial t^2} \end{array}, \tag{21c}$$

$$\delta w_{1c}: \begin{array}{c} \frac{\partial \mathscr{R}_{xzc}}{\partial x} + \frac{\partial \mathscr{Q}_{xzc}}{\partial x} + \frac{\partial \mathscr{R}_{yzc}}{\partial y} + \frac{\partial \mathscr{Q}_{yzc}}{\partial y} - \frac{\partial^2 \mathscr{P}_{xxc}}{\partial x^2} - \frac{\partial^2 \mathscr{P}_{yyc}}{\partial y^2} - \mathscr{S}_{zzc} - 2 \frac{\partial^2 \mathscr{P}_{xyc}}{\partial x \partial y} + \frac{\partial \mathscr{R}_{xzp}}{\partial x} \\ + \frac{\partial \mathscr{R}_{yzp}}{\partial y} - \frac{\partial^2 \mathscr{P}_{xxp}}{\partial x^2} - \frac{\partial^2 \mathscr{P}_{yyp}}{\partial y^2} - 2 \frac{\partial^2 \mathscr{P}_{xyp}}{\partial x \partial y} = \mathscr{I}_{1c} \frac{\partial^2 w_{oc}}{\partial t^2} + \mathscr{I}_{2c} \frac{\partial^2 w_{1c}}{\partial t^2} + \mathscr{O}_{1p} \frac{\partial^2 w_{op}}{\partial t^2} \\ + \mathscr{O}_{2p} \frac{\partial^2 w_{1p}}{\partial t^2} + \frac{\partial}{\partial x} \left(\mathscr{K}_{0cx} \frac{\partial^2 u_{oc}}{\partial t^2} \right) - \frac{\partial}{\partial x} \left(\mathscr{K}_{1cx} \frac{\partial^3 w_{oc}}{\partial x \partial t^2} \right) + \frac{\partial}{\partial x} \left(\mathscr{K}_{2cx} \frac{\partial^3 w_{1c}}{\partial x \partial t^2} \right) \\ + \frac{\partial}{\partial y} \left(\mathscr{K}_{0c} \frac{\partial^2 v_{0c}}{\partial t^2} \right) - \frac{\partial}{\partial y} \left(\mathscr{K}_{1c} \frac{\partial^3 w_{0c}}{\partial y \partial t^2} \right) + \frac{\partial}{\partial y} \left(\mathscr{K}_{2c} \frac{\partial^3 w_{1c}}{\partial y \partial t^2} \right) + \mathscr{K}_{0p} \frac{\partial^3 w_{0c}}{\partial x \partial t^2} \\ - \mathscr{K}_{1p} \frac{\partial^4 w_{0c}}{\partial x^2 \partial t^2} + \mathscr{K}_{2p} \frac{\partial^4 w_{1c}}{\partial x^2 \partial t^2} + \mathscr{K}_{3p} \frac{\partial^2 u_{1p}}{\partial t^2} + \mathscr{K}_{0p} \frac{\partial^3 v_{0c}}{\partial x \partial t^2} - \mathscr{K}_{1p} \frac{\partial^4 w_{0c}}{\partial y^2 \partial t^2} \\ + \mathscr{K}_{2p} \frac{\partial^4 w_{1c}}{\partial y^2 \partial t^2} + \mathscr{K}_{3p} \frac{\partial^2 v_{1p}}{\partial t^2} \end{array}, \tag{21d}$$

$$\delta u_{1p}: \frac{\partial \mathscr{Q}_{xzp}}{\partial x} + \frac{\partial \mathscr{Q}_{xyp}}{\partial y} - \mathscr{N}_{xzp} = \mathscr{I}_{0p} \frac{\partial^2 u_{0p}}{\partial t^2} - \mathscr{I}_{1p} \frac{\partial^3 w_{0p}}{\partial x \partial t^2} + \mathscr{I}_{2p} \frac{\partial^3 w_{1p}}{\partial x \partial t^2} + \mathscr{I}_{3p} \frac{\partial^2 u_{1p}}{\partial t^2}, \tag{21e}$$

Table 1
The TD-FGMs rectangular plate's material properties [45].

Ceramic (Al_2O_3)	Metal (SUS304)
$\mathbb{E}_c = 348.43 \times 10^9 [pa]$	$\mathbb{E}_m = 201.04 \times 10^9 [pa]$
$\nu_c = 0.2400$	$\nu_m = 0.3262$
$\rho_c = 2370 \left[\frac{Kg}{m^3}\right]$	$\rho_m = 8166 \left[\frac{Kg}{m^3}\right]$

$$\delta v_{1p} : \frac{\partial \mathscr{Q}_{yyp}}{\partial y} + \frac{\partial \mathscr{Q}_{xyp}}{\partial x} - \mathscr{N}_{yzp} = \mathscr{J}_{0p}\frac{\partial^2 v_{0p}}{\partial t^2} - \mathscr{J}_{1p}\frac{\partial^3 w_{0p}}{\partial y \partial t^2} + \mathscr{J}_{2p}\frac{\partial^3 w_{1p}}{\partial y \partial t^2} + \mathscr{J}_{3p}\frac{\partial^2 v_{1p}}{\partial t^2}, \tag{21f}$$

$$\delta\phi \quad : \quad \int_V \left\{ \frac{\partial \mathscr{D}_x}{\partial x}\cos(\beta z) + \frac{\partial \mathscr{D}_y}{\partial y}\cos(\beta z) + \beta \mathscr{D}_z \sin(\beta z) \right\} = 0. \tag{21g}$$

The definition of the matching boundary conditions is:

$$\delta u_{0c} = 0 \text{ or } \left(\mathscr{N}_{xxc} + \mathscr{N}_{xxp}\right)\widehat{n}_x + \left(\mathscr{N}_{xyc} + \mathscr{N}_{xyp}\right)\widehat{n}_y = 0, \tag{22a}$$

$$\delta v_{0c} = 0 \quad \text{or} \quad \left(\mathscr{N}_{xyc} + \mathscr{N}_{xyp}\right)\widehat{n}_x + \left(\mathscr{N}_{yyc} + \mathscr{N}_{yyp}\right)\widehat{n}_y = 0, \tag{22b}$$

$$\delta w_{0c} = 0 \quad \text{or} \quad \begin{aligned} &\left(\frac{\partial \mathscr{M}_{xxc}}{\partial x} + \frac{\partial \mathscr{M}_{xyc}}{\partial y} + \frac{\partial \mathscr{M}_{xxp}}{\partial x} + \frac{\partial \mathscr{M}_{xyp}}{\partial y} + \mathscr{N}_{xzp} + \mathscr{N}_{\mathscr{P}}\frac{\partial w_{0c}}{\partial x}\right)\widehat{n}_x \\ &+ \left(\frac{\partial \mathscr{M}_{yyc}}{\partial y} + \frac{\partial \mathscr{M}_{xyc}}{\partial x} + \frac{\partial \mathscr{M}_{yyp}}{\partial y} + \frac{\partial \mathscr{M}_{xyp}}{\partial x} + \mathscr{N}_{yzp} + \mathscr{N}_{\mathscr{P}}\frac{\partial w_{0c}}{\partial y}\right)\widehat{n}_y = 0 \end{aligned}, \tag{22c}$$

$$\delta w_{1c} = 0 \quad \text{or} \quad \begin{aligned} &\left(-\frac{\partial \mathscr{P}_{xxc}}{\partial x} - \frac{\partial \mathscr{P}_{xyc}}{\partial y} + \mathscr{R}_{xzc} + \mathscr{Q}_{xzc} - \frac{\partial \mathscr{P}_{xxp}}{\partial x} - \frac{\partial \mathscr{P}_{xyp}}{\partial y} + \mathscr{R}_{xzp}\right)\widehat{n}_x \\ &+ \left(-\frac{\partial \mathscr{P}_{yyc}}{\partial y} - \frac{\partial \mathscr{P}_{xyc}}{\partial x} + \mathscr{R}_{yzc} + \mathscr{Q}_{yzc} - \frac{\partial \mathscr{P}_{yyp}}{\partial y} - \frac{\partial \mathscr{P}_{xyp}}{\partial x} + \mathscr{R}_{yzp}\right)\widehat{n}_y = 0 \end{aligned}, \tag{22d}$$

$$\delta u_{1p} = 0 \text{ or } \left(\mathscr{Q}_{xzp}\right)\widehat{n}_x + \left(\mathscr{Q}_{xyp}\right)\widehat{n}_y = 0, \tag{22e}$$

Table 4
Comparison of first dimensionless fundamental frequencies of functionally graded nanoplates with respect to nonlocality, plate's aspect ratio, and its length-to-thickness ratio.

a/b	$\mu(nm^2)$	$a/h = 10$		$a/h = 20$	
		Present	Ref. [50]	Present	Ref. [50]
1	0	0.0460	0.0441	0.0115	0.0113
	1	0.0420	0.0403	0.0105	0.0103
	2	0.0389	0.0374	0.0097	0.0096
	4	0.0343	0.0330	0.0085	0.0085
2	0	0.1135	0.1055	0.0286	0.0279
	1	0.0928	0.0863	0.0235	0.0229
	2	0.0804	0.0748	0.0202	0.0198
	4	0.0657	0.0612	0.0165	0.0162

$$\delta v_{1p} = 0 \text{ or } \left(\mathscr{Q}_{xyp}\right)\widehat{n}_x + \left(\mathscr{Q}_{yyp}\right)\widehat{n}_y = 0, \tag{22f}$$

$$\delta\phi = 0\,, \tag{22g}$$

$$\frac{\partial \delta w_{0c}}{\partial x} = 0 \quad \text{or} \quad \left(\mathscr{M}_{xxc} + \mathscr{M}_{xxp}\right)\widehat{n}_x + \left(\mathscr{M}_{xyc} + \mathscr{M}_{xyp}\right)\widehat{n}_y = 0\,, \tag{22h}$$

$$\frac{\partial \delta w_{0c}}{\partial y} = 0 \quad \text{or} \quad \left(\mathscr{M}_{xyc} + \mathscr{M}_{xyp}\right)\widehat{n}_x + \left(\mathscr{M}_{yyc} + \mathscr{M}_{yyp}\right)\widehat{n}_y = 0\,, \tag{22i}$$

$$\frac{\partial \delta w_{1c}}{\partial x} = 0 \quad \text{or} \quad \left(\mathscr{P}_{xxc} + \mathscr{P}_{xxp}\right)\widehat{n}_x + \left(\mathscr{P}_{xyc} + \mathscr{P}_{xyp}\right)\widehat{n}_y = 0\,, \tag{22j}$$

$$\frac{\partial \delta w_{0c}}{\partial y} = 0 \quad \text{or} \quad \left(\mathscr{P}_{xyc} + \mathscr{P}_{xyp}\right)\widehat{n}_x + \left(\mathscr{P}_{yyc} + \mathscr{P}_{yyp}\right)\widehat{n}_y = 0\,. \tag{22k}$$

where

Table 2
The PZT-4 material characteristics [46].

$\mathfrak{Q}_{11}$ [GPa]	$\mathfrak{Q}_{22}$ [GPa]	$\mathfrak{Q}_{12}$ [GPa]	$\mathfrak{Q}_{13}$ [GPa]	$\mathfrak{Q}_{33}$ [GPa]	$\mathfrak{Q}_{44}$ [GPa]	$\mathfrak{Q}_{55}$ [GPa]	$\mathfrak{Q}_{66}$ [GPa]
132	132	71	73	115	26	26	30.5
e_{31} $[C/m^2]$	e_{32} $[C/m^2]$	e_{33} $[C/m^2]$	e_{15} $[C/m^2]$	e_{24} $[C/m^2]$	$\mathscr{T}_{11}$ [C/Vm]	$\mathscr{T}_{22}$ [C/Vm]	$\mathscr{T}_{33}$ [C/Vm]
− 4.1	− 4.1	14.1	10.5	10.5	5.841×10^{-9}	5.841×10^{-9}	7.124×10^{-9}
ρ $[Kg/m^3]$							
7500							

Table 3
Comparison of present results for the circular frequencies (ω) with the results of Ref. [1–3] (ν =0.3, E = 210 [GPa], ρ = 7480 [Kg/m^3], h = 0.01 [m])

Mode number	$k = 2$	$k = 5$	$k = 8$	$k = 11$	$k = 14$	$k = 17$	$k = 20$	$k = 23$
Present	128.22	800.65	2047.20	3862.74	6239.53	9169.50	12641.10	16641.41
Ref. [47]	128.46	802.28	2050.90	3869.44	6250.88	9186.18	12664.47	16673.20
Ref. [48]	128.27	801.71	2052.38	3880.28	6285.41	9267.77	12827.37	16964.19
Ref. [49]	128.26	800.97	2047.55	3863.09	6240.55	9170.85	12643.1	16644.5

$$
\begin{aligned}
&\{\mathscr{N}_{xx\mathrm{c}},\mathscr{M}_{xx\mathrm{c}},\mathscr{P}_{xx\mathrm{c}},\mathscr{Q}_{xx\mathrm{c}},\mathscr{R}_{xx\mathrm{c}},\mathscr{S}_{xx\mathrm{c}}\}=\int_V(\{1,z,\mathscr{f}(z),\,\mathscr{G}(z),\mathscr{f}_1(z),\,\mathscr{G}_1(z)\}\sigma_{xx\mathrm{c}})\mathrm{d}x\mathrm{d}y\mathrm{d}z,\\
&\{\mathscr{N}_{yy\mathrm{c}},\mathscr{M}_{yy\mathrm{c}},\mathscr{P}_{yy\mathrm{c}},\mathscr{Q}_{yy\mathrm{c}},\mathscr{R}_{yy\mathrm{c}},\mathscr{S}_{yy\mathrm{c}}\}=\int_V\left(\{1,z,\mathscr{f}(z),\,\mathscr{G}(z),\mathscr{f}_1(z),\,\mathscr{G}_1(z)\}\sigma_{yy\mathrm{c}}\right)\mathrm{d}x\mathrm{d}y\mathrm{d}z,\\
&\{\mathscr{N}_{zz\mathrm{c}},\mathscr{M}_{zz\mathrm{c}},\mathscr{P}_{zz\mathrm{c}},\mathscr{Q}_{zz\mathrm{c}},\mathscr{R}_{zz\mathrm{c}},\mathscr{S}_{zz\mathrm{c}}\}=\int_V(\{1,z,\mathscr{f}(z),\,\mathscr{G}(z),\mathscr{f}_1(z),\,\mathscr{G}_1(z)\}\sigma_{zz\mathrm{c}})\mathrm{d}x\mathrm{d}y\mathrm{d}z,\\
&\{\mathscr{N}_{yz\mathrm{c}},\mathscr{M}_{yz\mathrm{c}},\mathscr{P}_{yz\mathrm{c}},\mathscr{Q}_{yz\mathrm{c}},\mathscr{R}_{yz\mathrm{c}},\mathscr{S}_{yz\mathrm{c}}\}=\int_V\left(\{1,z,\mathscr{f}(z),\,\mathscr{G}(z),\mathscr{f}_1(z),\,\mathscr{G}_1(z)\}\sigma_{yz\mathrm{c}}\right)\mathrm{d}x\mathrm{d}y\mathrm{d}z,\\
&\{\mathscr{N}_{xz\mathrm{c}},\mathscr{M}_{xz\mathrm{c}},\mathscr{P}_{xz\mathrm{c}},\mathscr{Q}_{xz\mathrm{c}},\mathscr{R}_{xz\mathrm{c}},\mathscr{S}_{xz\mathrm{c}}\}=\int_V(\{1,z,\mathscr{f}(z),\,\mathscr{G}(z),\mathscr{f}_1(z),\,\mathscr{G}_1(z)\}\sigma_{xz\mathrm{c}})\mathrm{d}x\mathrm{d}y\mathrm{d}z,\\
&\{\mathscr{N}_{xy\mathrm{c}},\mathscr{M}_{xy\mathrm{c}},\mathscr{P}_{xy\mathrm{c}},\mathscr{Q}_{xy\mathrm{c}},\mathscr{R}_{xy\mathrm{c}},\mathscr{S}_{xy\mathrm{c}}\}=\int_V\left(\{1,z,\mathscr{f}(z),\,\mathscr{G}(z),\mathscr{f}_1(z),\,\mathscr{G}_1(z)\}\sigma_{xy\mathrm{c}}\right)\mathrm{d}x\mathrm{d}y\mathrm{d}z,\\
&\{\mathscr{N}_{xx\mathrm{p}},\mathscr{M}_{xx\mathrm{p}},\mathscr{P}_{xx\mathrm{p}},\mathscr{Q}_{xx\mathrm{p}},\mathscr{R}_{xx\mathrm{p}}\}=\int_V\left(\left\{1,\left(\frac{h_c}{2}\right),\mathscr{f}\left(\frac{h_c}{2}\right),\left(z-\frac{h_c}{2}\right),\,\mathscr{G}\left(\frac{h_c}{2}\right)\right\}\sigma_{xx\mathrm{p}}\right)\mathrm{d}x\mathrm{d}y\mathrm{d}z,\\
&\{\mathscr{N}_{yy\mathrm{p}},\mathscr{M}_{yy\mathrm{p}},\mathscr{P}_{yy\mathrm{p}},\mathscr{Q}_{yy\mathrm{p}},\mathscr{R}_{yy\mathrm{p}}\}=\int_V\left(\left\{1,\left(\frac{h_c}{2}\right),\mathscr{f}\left(\frac{h_c}{2}\right),\left(z-\frac{h_c}{2}\right),\,\mathscr{G}\left(\frac{h_c}{2}\right)\right\}\sigma_{yy\mathrm{p}}\right)\mathrm{d}x\mathrm{d}y\mathrm{d}z,\\
&\{\mathscr{N}_{zz\mathrm{p}},\mathscr{M}_{zz\mathrm{p}},\mathscr{P}_{zz\mathrm{p}},\mathscr{Q}_{zz\mathrm{p}},\mathscr{R}_{zz\mathrm{p}}\}=\int_V\left(\left\{1,\left(\frac{h_c}{2}\right),\mathscr{f}\left(\frac{h_c}{2}\right),\left(z-\frac{h_c}{2}\right),\,\mathscr{G}\left(\frac{h_c}{2}\right)\right\}\sigma_{zz\mathrm{p}}\right)\mathrm{d}x\mathrm{d}y\mathrm{d}z,\\
&\{\mathscr{N}_{yz\mathrm{p}},\mathscr{M}_{yz\mathrm{p}},\mathscr{P}_{yz\mathrm{p}},\mathscr{Q}_{yz\mathrm{p}},\mathscr{R}_{yz\mathrm{p}}\}=\int_V\left(\left\{1,\left(\frac{h_c}{2}\right),\mathscr{f}\left(\frac{h_c}{2}\right),\left(z-\frac{h_c}{2}\right),\,\mathscr{G}\left(\frac{h_c}{2}\right)\right\}\sigma_{yz\mathrm{p}}\right)\mathrm{d}x\mathrm{d}y\mathrm{d}z,\\
&\{\mathscr{N}_{xz\mathrm{p}},\mathscr{M}_{xz\mathrm{p}},\mathscr{P}_{xz\mathrm{p}},\mathscr{Q}_{xz\mathrm{p}},\mathscr{R}_{xz\mathrm{p}}\}=\int_V\left(\left\{1,\left(\frac{h_c}{2}\right),\mathscr{f}\left(\frac{h_c}{2}\right),\left(z-\frac{h_c}{2}\right),\,\mathscr{G}\left(\frac{h_c}{2}\right)\right\}\sigma_{xz\mathrm{p}}\right)\mathrm{d}x\mathrm{d}y\mathrm{d}z,\\
&\{\mathscr{N}_{xy\mathrm{p}},\mathscr{M}_{xy\mathrm{p}},\mathscr{P}_{xy\mathrm{p}},\mathscr{Q}_{xy\mathrm{p}},\mathscr{R}_{xy\mathrm{p}}\}=\int_V\left(\left\{1,\left(\frac{h_c}{2}\right),\mathscr{f}\left(\frac{h_c}{2}\right),\left(z-\frac{h_c}{2}\right),\,\mathscr{G}\left(\frac{h_c}{2}\right)\right\}\sigma_{xy\mathrm{p}}\right)\mathrm{d}x\mathrm{d}y\mathrm{d}z,\\
&\{\mathscr{I}_{0c},\mathscr{I}_{1c},\mathscr{I}_{2c}\}=\int_V(\{1,z,\mathscr{f}(z)\}\rho_c(x,y,z))\mathrm{d}x\mathrm{d}y\mathrm{d}z,\\
&\{\mathscr{L}_{0c},\mathscr{L}_{1c},\mathscr{L}_{2c}\}=\int_V\left(\left\{z,z^2,z\mathscr{f}(z)\right\}\rho_c(x,y,z)\right)\mathrm{d}x\mathrm{d}y\mathrm{d}z,\\
&\{\mathscr{K}_{0c},\mathscr{K}_{1c},\mathscr{K}_{2c}\}=\int_V\left(\mathscr{f}(z),z\mathscr{f}(z),\mathscr{f}^2(z)\rho_c(x,y,z)\right)\mathrm{d}x\mathrm{d}y\mathrm{d}z,\\
&\{\mathscr{J}_{0c},\mathscr{J}_{1c},\mathscr{J}_{2c}\}=\int_V\left(\left\{1,\,\mathscr{G}(z),\,\mathscr{G}^2(z)\right\}\rho_c(x,y,z)\right)\mathrm{d}x\mathrm{d}y\mathrm{d}z,\\
&\{\mathscr{I}_{0p},\mathscr{I}_{1p},\mathscr{I}_{2p},\mathscr{I}_{3p}\}=\int_V\left(\left\{1,\left(\frac{h_c}{2}\right),\mathscr{f}\left(\frac{h_c}{2}\right),\left(z-\frac{h_c}{2}\right)\right\}\rho_p\right)\mathrm{d}x\mathrm{d}y\mathrm{d}z,\\
&\{\mathscr{L}_{0p},\mathscr{L}_{1p},\mathscr{L}_{2p},\mathscr{L}_{3p}\}=\int_V\left(\left\{\left(\frac{h_c}{2}\right),\left(\frac{h_c}{2}\right)^2,\left(\frac{h_c}{2}\right)\mathscr{f}\left(\frac{h_c}{2}\right),\left(\frac{h_c}{2}\right)\left(z-\frac{h_c}{2}\right)\right\}\rho_c(x,y,z)\right)\mathrm{d}x\mathrm{d}y\mathrm{d}z,\\
&\{\mathscr{K}_{0p},\mathscr{K}_{1p},\mathscr{K}_{2p},\mathscr{K}_{3p}\}=\int_V\left(\left\{\mathscr{f}\left(\frac{h_c}{2}\right),\left(\frac{h_c}{2}\right)\mathscr{f}\left(\frac{h_c}{2}\right),\mathscr{f}^2\left(\frac{h_c}{2}\right),\mathscr{f}\left(\frac{h_c}{2}\right)\left(z-\frac{h_c}{2}\right)\right\}\rho_p\right)\mathrm{d}x\mathrm{d}y\mathrm{d}z,\\
&\{\mathscr{J}_{0p},\mathscr{J}_{1p},\mathscr{J}_{2p},\mathscr{J}_{3p}\}=\int_V\left(\left\{\left(z-\frac{h_c}{2}\right),\left(\frac{h_c}{2}\right)\left(z-\frac{h_c}{2}\right),\left(z-\frac{h_c}{2}\right)\mathscr{f}\left(\frac{h_c}{2}\right),\left(z-\frac{h_c}{2}\right)^2\right\}\rho_{\mathscr{P}}\right)\mathrm{d}x\mathrm{d}y\mathrm{d}z,\\
&\{\mathscr{O}_{0p},\mathscr{O}_{1p},\mathscr{O}_{2p}\}=\int_V\left(\left\{1,\,\mathscr{G}\left(\frac{h_c}{2}\right),\,\mathscr{G}^2\left(\frac{h_c}{2}\right)\right\}\rho_{\mathscr{P}}\right)\mathrm{d}x\mathrm{d}y\mathrm{d}z.
\end{aligned}
\tag{23}
$$

Eqs. (10), (12), and (13) are substituted into Eqs. (21a-g) to provide the equations of motion for the TD-FGMs reinforced nanoplate based on the general nonlocal strain gradient refined shear deformable theory in terms of displacement fields.

$$
\begin{gathered}
\left(1-l^2\nabla^2\right)\left(\frac{\partial \mathscr{N}_{xxc}}{\partial x}+\frac{\partial \mathscr{N}_{xyc}}{\partial y}+\frac{\partial \mathscr{N}_{xxp}}{\partial x}+\frac{\partial \mathscr{N}_{xyp}}{\partial y}\right)= \\
\delta u_{0c}\ :\quad \left(1-\mu^2\nabla^2\right)\left(\begin{array}{c}
\mathscr{I}_{0c}\dfrac{\partial^2 u_{0c}}{\partial t^2}-\mathscr{I}_{1c}\dfrac{\partial^3 w_{0c}}{\partial x\partial t^2}+\mathscr{I}_{2c}\dfrac{\partial^3 w_{1c}}{\partial x\partial t^2} \\
+\mathscr{I}_{0p}\dfrac{\partial^2 u_{0c}}{\partial t^2}-\mathscr{I}_{1p}\dfrac{\partial^3 w_{0c}}{\partial x\partial t^2}+\mathscr{I}_{2p}\dfrac{\partial^3 w_{1c}}{\partial x\partial t^2}+\mathscr{I}_{3p}\dfrac{\partial^2 u_{1c}}{\partial t^2}
\end{array}\right),
\end{gathered}
\tag{24a}
$$

$$
\begin{gathered}
\left(1-l^2\nabla^2\right)\left(\frac{\partial \mathscr{N}_{yyc}}{\partial y}+\frac{\partial \mathscr{N}_{xyc}}{\partial x}+\frac{\partial \mathscr{N}_{yyp}}{\partial y}+\frac{\partial \mathscr{N}_{xyp}}{\partial x}\right)= \\
\delta v_{0c}\ :\quad \left(1-\mu^2\nabla^2\right)\left(\begin{array}{c}
\mathscr{I}_{0c}\dfrac{\partial^2 v_{0c}}{\partial t^2}-\mathscr{I}_{1c}\dfrac{\partial^3 w_{0c}}{\partial y\partial t^2}+\mathscr{I}_{2c}\dfrac{\partial^3 w_{1c}}{\partial y\partial t^2} \\
+\mathscr{I}_{0p}\dfrac{\partial^2 v_{0c}}{\partial t^2}-\mathscr{I}_{1p}\dfrac{\partial^3 w_{0c}}{\partial y\partial t^2}+\mathscr{I}_{2p}\dfrac{\partial^3 w_{1c}}{\partial y\partial t^2}+\mathscr{I}_{3p}\dfrac{\partial^2 v_{1c}}{\partial t^2}
\end{array}\right),
\end{gathered}
\tag{24b}
$$

$$
\begin{gathered}
\left(1-l^2\nabla^2\right)\left(\begin{array}{c}
\dfrac{\partial^2 \mathscr{M}_{xxc}}{\partial x^2}+\dfrac{\partial^2 \mathscr{M}_{yyc}}{\partial y^2}+2\dfrac{\partial^2 \mathscr{M}_{xyc}}{\partial x\partial y}+\dfrac{\partial^2 \mathscr{M}_{xxp}}{\partial x^2}+\dfrac{\partial^2 \mathscr{M}_{yyp}}{\partial y^2} \\
+2\dfrac{\partial^2 \mathscr{M}_{xyp}}{\partial x\partial y}+\dfrac{\partial \mathscr{N}_{xzp}}{\partial x}+\dfrac{\partial \mathscr{N}_{yzp}}{\partial y}+2\dfrac{\partial^2 \mathscr{M}_{xyp}}{\partial x\partial y}
\end{array}\right) \\
-\mathscr{N}_{\mathscr{P}}\left(1-\mu^2\nabla^2\right)\left(\frac{\partial^2 w_{0c}}{\partial x^2}+\frac{\partial^2 w_{0c}}{\partial y^2}\right)=\left(1-\mu^2\nabla^2\right)\times \\
\delta w_{0c}:\left(\begin{array}{c}
\mathscr{I}_{0c}\dfrac{\partial^2 w_{0c}}{\partial t^2}+\mathscr{I}_{1c}\dfrac{\partial^2 w_{1c}}{\partial t^2}+\mathscr{O}_{0p}\dfrac{\partial^2 w_{p}}{\partial t^2}+\mathscr{O}_{1p}\dfrac{\partial^2 w_{1p}}{\partial t^2}-\dfrac{\partial}{\partial x}\left(\mathscr{L}_{0cx}\dfrac{\partial^2 u_{0c}}{\partial t^2}\right) \\
+\dfrac{\partial}{\partial x}\left(\mathscr{L}_{1cx}\dfrac{\partial^3 w_{0c}}{\partial x\partial t^2}\right)-\dfrac{\partial}{\partial x}\left(\mathscr{L}_{2cx}\dfrac{\partial^3 w_{1c}}{\partial x\partial t^2}\right)-\dfrac{\partial}{\partial y}\left(\mathscr{L}_{0c}\dfrac{\partial^2 v_{0c}}{\partial t^2}\right)+\dfrac{\partial}{\partial y}\left(\mathscr{L}_{1c}\dfrac{\partial^3 w_{0c}}{\partial y\partial t^2}\right) \\
-\dfrac{\partial}{\partial y}\left(\mathscr{L}_{2c}\dfrac{\partial^3 w_{1c}}{\partial y\partial t^2}\right)-\mathscr{L}_{0p}\dfrac{\partial^3 u_{0c}}{\partial x\partial t^2}+\mathscr{L}_{1p}\dfrac{\partial^4 w_{0c}}{\partial x^2\partial t^2}-\mathscr{L}_{2p}\dfrac{\partial^4 w_{1c}}{\partial x^2\partial t^2}-\mathscr{L}_{3p}\dfrac{\partial^2 u_{1p}}{\partial t^2} \\
-\mathscr{L}_{0p}\dfrac{\partial^3 v_{0c}}{\partial x\partial t^2}+\mathscr{L}_{1p}\dfrac{\partial^4 w_{0c}}{\partial y^2\partial t^2}-\mathscr{L}_{2p}\dfrac{\partial^4 w_{1c}}{\partial y^2\partial t^2}-\mathscr{L}_{3p}\dfrac{\partial^2 v_{1p}}{\partial t^2}
\end{array}\right),
\end{gathered}
\tag{24c}
$$

$$
\begin{gathered}
\left(1-l^2\nabla^2\right)\left(\begin{array}{c}
\dfrac{\partial \mathscr{R}_{xzc}}{\partial x}+\dfrac{\partial \mathscr{Q}_{xzc}}{\partial x}+\dfrac{\partial \mathscr{R}_{yzc}}{\partial y}+\dfrac{\partial \mathscr{Q}_{yzc}}{\partial y}-\dfrac{\partial^2 \mathscr{P}_{xxc}}{\partial x^2}-\dfrac{\partial^2 \mathscr{P}_{yyc}}{\partial y^2}-\mathscr{S}_{zzc} \\
-2\dfrac{\partial^2 \mathscr{P}_{xyc}}{\partial x\partial y}+\dfrac{\partial \mathscr{R}_{xzp}}{\partial x}+\dfrac{\partial \mathscr{R}_{yzp}}{\partial y}-\dfrac{\partial^2 \mathscr{P}_{xxp}}{\partial x^2}-\dfrac{\partial^2 \mathscr{P}_{yyp}}{\partial y^2}-2\dfrac{\partial^2 \mathscr{P}_{xyp}}{\partial x\partial y}
\end{array}\right) \\
=\left(1-\mu^2\nabla^2\right)\times \\
\delta w_{1c}:\left(\begin{array}{c}
\mathscr{J}_{1c}\dfrac{\partial^2 w_{0c}}{\partial t^2}+\mathscr{J}_{2c}\dfrac{\partial^2 w_{1c}}{\partial t^2}+\mathscr{O}_{1p}\dfrac{\partial^2 w_{0p}}{\partial t^2}+\mathscr{O}_{2p}\dfrac{\partial^2 w_{1p}}{\partial t^2}+\dfrac{\partial}{\partial x}\left(\mathscr{K}_{0cx}\dfrac{\partial^2 u_{0c}}{\partial t^2}\right) \\
-\dfrac{\partial}{\partial x}\left(\mathscr{K}_{1cx}\dfrac{\partial^3 w_{0c}}{\partial x\partial t^2}\right)+\dfrac{\partial}{\partial x}\left(\mathscr{K}_{2cx}\dfrac{\partial^3 w_{1c}}{\partial x\partial t^2}\right)+\dfrac{\partial}{\partial y}\left(\mathscr{K}_{0c}\dfrac{\partial^2 v_{0c}}{\partial t^2}\right)-\dfrac{\partial}{\partial y}\left(\mathscr{K}_{1c}\dfrac{\partial^3 w_{0c}}{\partial y\partial t^2}\right) \\
+\dfrac{\partial}{\partial y}\left(\mathscr{K}_{2c}\dfrac{\partial^3 w_{1c}}{\partial y\partial t^2}\right)+\mathscr{K}_{0p}\dfrac{\partial^3 u_{0c}}{\partial x\partial t^2}-\mathscr{K}_{1p}\dfrac{\partial^4 w_{0c}}{\partial x^2\partial t^2}+\mathscr{K}_{2p}\dfrac{\partial^4 w_{1c}}{\partial x^2\partial t^2}+\mathscr{K}_{3p}\dfrac{\partial^2 u_{1p}}{\partial t^2} \\
+\mathscr{K}_{0p}\dfrac{\partial^3 v_{0c}}{\partial x\partial t^2}-\mathscr{K}_{1p}\dfrac{\partial^4 w_{0c}}{\partial y^2\partial t^2}+\mathscr{K}_{2p}\dfrac{\partial^4 w_{1c}}{\partial y^2\partial t^2}+\mathscr{K}_{3p}\dfrac{\partial^2 v_{1p}}{\partial t^2}
\end{array}\right),
\end{gathered}
\tag{24d}
$$

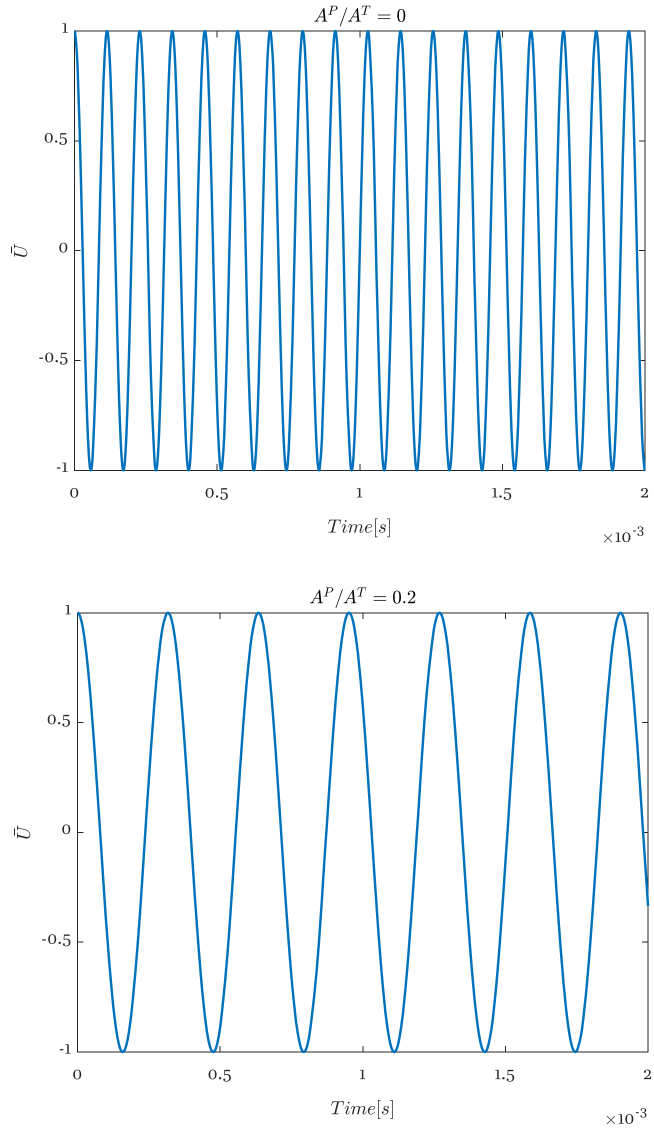

Fig. 3. The influence of the A^P to A^T ratio of the structure to the energy absorption capacity ($\overline{U} = \frac{U}{U_{max}}$) of the presented composite structure.

$$\delta u_{1p} \quad : \quad \begin{array}{c} (1 - l^2\nabla^2)\left(\dfrac{\partial \mathscr{Q}_{xzp}}{\partial x} + \dfrac{\partial \mathscr{Q}_{xyp}}{\partial y} - \mathscr{N}_{xzp}\right) = \\ (1 - \mu^2\nabla^2)\left(\mathscr{I}_{0p}\dfrac{\partial^2 u_{0p}}{\partial t^2} - \mathscr{I}_{1p}\dfrac{\partial^3 w_{0p}}{\partial x \partial t^2} + \mathscr{I}_{2p}\dfrac{\partial^3 w_{1p}}{\partial x \partial t^2} + \mathscr{I}_{3p}\dfrac{\partial^2 u_{1p}}{\partial t^2}\right) \end{array}, \tag{24e}$$

$$\delta v_{1p} \quad : \quad \begin{array}{c} (1 - l^2\nabla^2)\left(\dfrac{\partial \mathscr{Q}_{yyp}}{\partial y} + \dfrac{\partial \mathscr{Q}_{xyp}}{\partial x} - \mathscr{N}_{yzp}\right) = \\ (1 - \mu^2\nabla^2)\left(\mathscr{I}_{0p}\dfrac{\partial^2 v_{0p}}{\partial t^2} - \mathscr{I}_{1p}\dfrac{\partial^3 w_{0p}}{\partial y \partial t^2} + \mathscr{I}_{2p}\dfrac{\partial^3 w_{1p}}{\partial y \partial t^2} + \mathscr{I}_{3p}\dfrac{\partial^2 v_{1p}}{\partial t^2}\right) \end{array}, \tag{24f}$$

$$\delta\phi \quad : \quad \int_V (1 - l^2\nabla^2)\left\{\frac{\partial \mathscr{D}_x}{\partial x}\cos(\beta z) + \frac{\partial \mathscr{D}_y}{\partial y}\cos(\beta z) + \beta\mathscr{D}_z\sin(\beta z)\right\} = 0. \tag{24g}$$

3. Solution procedure

Analytical solution methodology offers several advantages, especially in engineering, physics, and mathematics. First, it provides exact solutions, giving precise insights into the system's behavior without approximation. This is crucial for verifying numerical methods, as analytical solutions can serve as benchmarks for comparison. Second, analytical methods often yield closed-form expressions, allowing for deeper theoretical understanding. These expressions can reveal underlying relationships between variables, offer insights into parameter sensitivity, and predict system responses under various conditions without rerunning simulations. Another benefit is computational efficiency. Once an analytical solution is derived, it can be evaluated quickly without the need for iterative computations, making it ideal for real-time or embedded systems applications. Moreover, analytical solutions can lead to generalized solutions applicable to a wide range of problems with similar boundary conditions or governing equations, offering flexibility and scalability in problem-solving. However, analytical methods are often limited to relatively simple geometries and boundary conditions. Despite this, their ability to provide exact, insightful, and efficient solutions remains a valuable tool in theoretical and applied fields. It is advised to use the generic nonlocal strain gradient second-order shear deformation theory to solve the partial differential equations (PDEs) for the dynamic concerns in the previous section. PDEs will have analytical solutions obtained using a harmonic solution procedure. The following is a list of expressions:

$$\begin{aligned} &u_{0c} = \mathscr{U}_{0c}\exp(kx + ky - \omega t)i, v_{0c} = \mathscr{V}_{0c}\exp(kx + ky - \omega t)i, \\ &w_{0c} = \mathscr{W}_{0c}\exp(kx + ky - \omega t)i, w_{1c} = \mathscr{W}_{1c}\exp(kx + ky - \omega t)i, \\ &u_{1p} = \mathscr{U}_{1p}\exp(kx + ky - \omega t)i, v_{1p} = \mathscr{V}_{1p}\exp(kx + ky - \omega t)i, \end{aligned} \tag{25}$$

$$\phi = \overline{\phi}\exp(kx + ky - \omega t)i,$$

where wave number and natural frequency are denoted by k, and ω. Furthermore, $i = \sqrt{-1}$. Next, by inserting Eqs. (23), and (25) into Eqs. (24a-g) we have:

$$\{[\mathscr{K}] - [\mathscr{M}]\omega^2\}\{\mathfrak{X}\} = 0, \tag{26}$$

where

$$\mathfrak{X} = \begin{bmatrix} \mathscr{U}_{0c} & \mathscr{V}_{0c} & \mathscr{W}_{0c} & \mathscr{W}_{1c} & \mathscr{U}_{1p} & \mathscr{V}_{1p} & \overline{\phi} \end{bmatrix}^T. \tag{27}$$

By solving Eq. (26), the eigenvalue and eigenvector of the structure may be achieved.

Also, the phase velocity may be computed by Eq. (28)

$$phase\ velocity = \frac{\omega}{k}. \tag{28}$$

4. Introduction of AI to predict the mentioned problem using appropriate datasets of mathematics simulation

In the context of validating vibrations and energy capacity in tri-directional functionally graded (FG) nanoplates attached to piezoelectric patches, artificial intelligence (AI) offers a powerful tool to optimize and verify complex mathematical simulations. The use of AI, particularly through machine learning (ML) models, can assist in identifying patterns, refining predictions, and enhancing the accuracy of the simulation results [43,44].

For this purpose, AI can leverage large datasets generated from finite element methods (FEM), meshless methods, or other computational simulations to train predictive models. These models can validate the vibrational characteristics and energy harvesting capacity by learning from the input-output relationships in the dataset, including factors like material gradation, and boundary conditions.

Typical AI approaches that might be used include:

- Regression Models: These can predict natural frequencies and energy output based on known parameters, helping to verify whether the simulations align with real-world results.

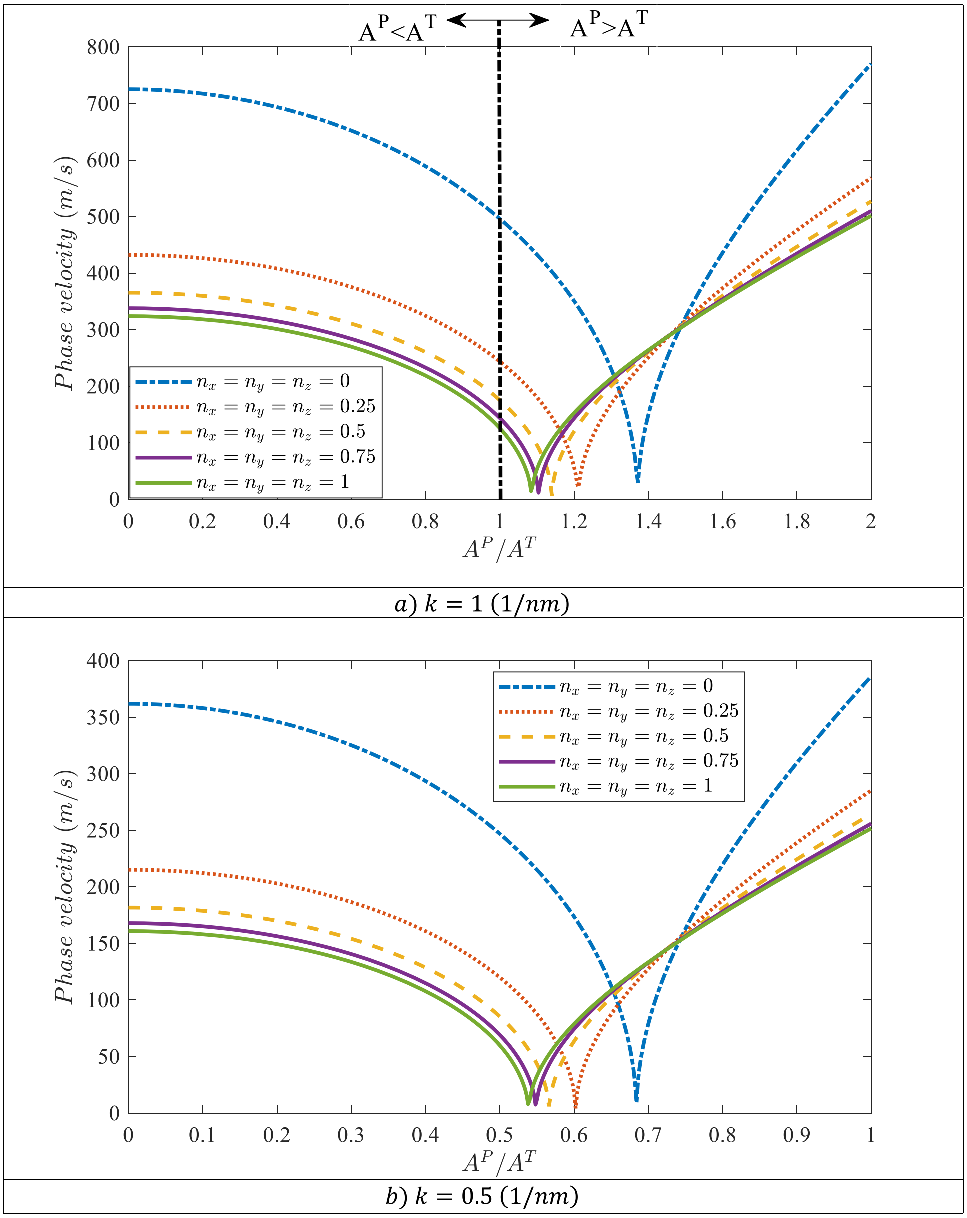

Fig. 4. The effect of the gradient index of the functionally graded (metal-ceramic) plate on the phase velocity as a function of the piezoelectric patch area to rectangular FG plate area ratio for $h = 0.1(nm)$, $b = a$, $a = 10h$, $l = \frac{h}{10}$, $\mu = \frac{h}{10}$, and $\varnothing_0 = 1(mV)$.

- Neural Networks: Deep learning models, such as deep neural networks (DNN), can model complex relationships between the FG nanoplate's vibrational modes and the applied piezoelectric effect, providing highly accurate validation results.
- Optimization Algorithm: Methods like particle swarm optimization (PSO) or genetic algorithm can fine-tune simulation parameters, ensuring that the modeled results (vibration frequencies and energy capacity) align with experimental or benchmarked data.
- AI-Based Sensitivity Analysis: AI techniques can help perform sensitivity analyses, identifying which parameters most influence the vibrational response and energy capacity of the nanoplate-piezoelectric system.

By incorporating AI into this process, the validation of simulation results can be more reliable, robust, and faster, providing insights into the mechanical and electrical behaviors of the FG nanoplate system. Using artificial intelligence (AI) to predict the vibrations and energy capacity of a tri-directional functionally graded (FG) nanoplate attached to a piezoelectric patch offers several advantages over traditional methods. These advantages stem from AI's ability to handle complex systems, manage large datasets, and optimize simulations efficiently.

1. Handling Complexities
   - **AI:** Can model and capture highly relationships between the parameters of the FG nanoplate (e.g., material gradation, thickness variation, geometric irregularities) and its vibrational and energy response. Neural networks, for example, can approximate complex functions without needing explicit equations.
   - **Traditional Methods:** Often require simplifying assumptions (such as linearization) to solve problems, which can lead to less accurate results.
2. Efficient Use of Large Datasets
   - AI: Utilizes machine learning models that can be trained on large datasets generated from finite element simulations or experimental data. Once trained, AI models can quickly predict outcomes

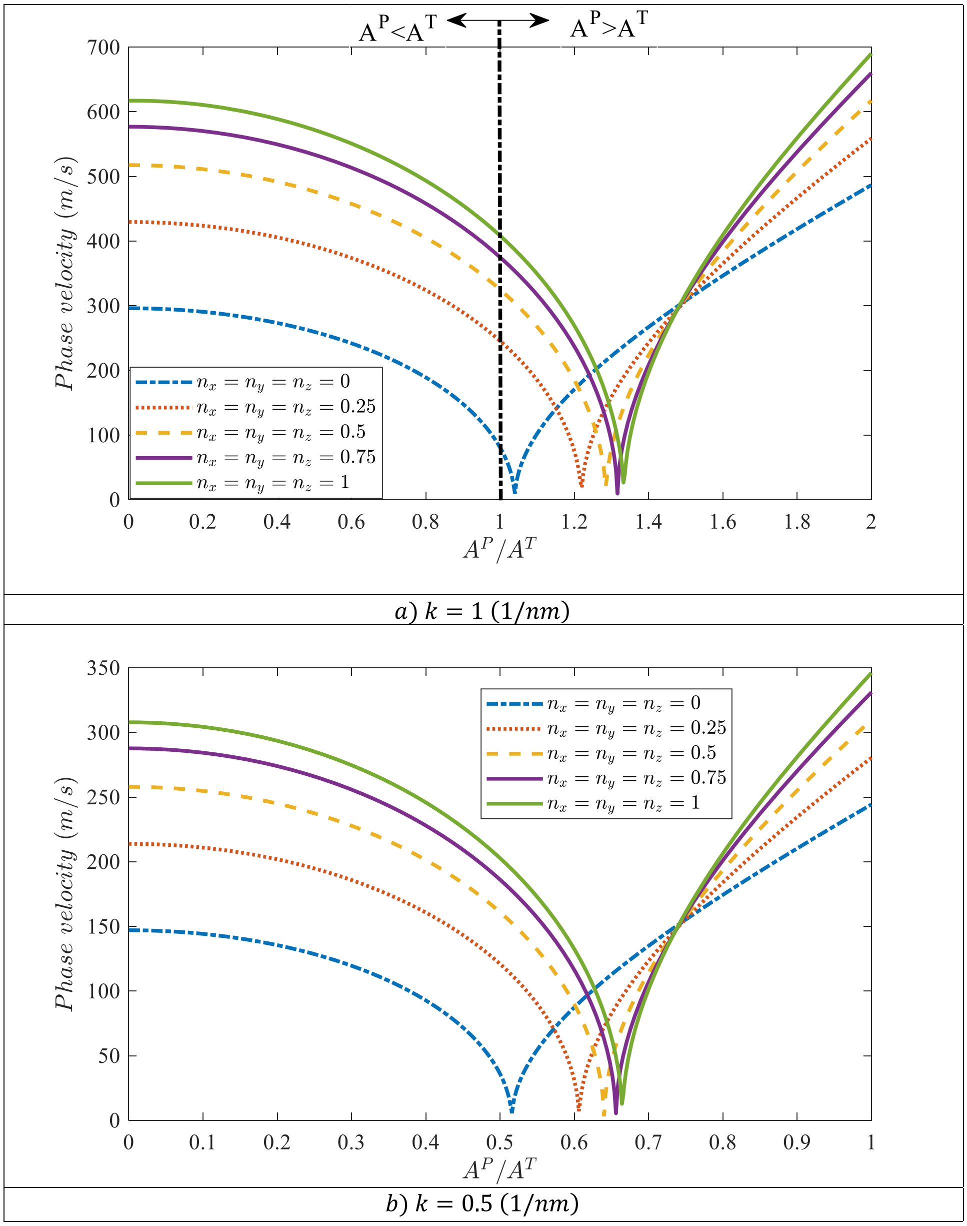

Fig. 5. The effect of the gradient index of the functionally graded (ceramic-metal) plate on the phase velocity as a function of the piezoelectric patch area to rectangular FG plate area ratio with $h = 0.1(nm)$, $b = a$, $a = 10h$, $l = \frac{h}{10}$, $\mu = \frac{h}{10}$, and $\varnothing_0 = 1(mV)$.

for new input configurations without needing to run time-consuming simulations.
- Traditional Methods: Require each new simulation or scenario to be solved from scratch, leading to long computation times, especially when using finite element or meshless methods for each case.

3. Faster Predictions
   - AI: After initial training, AI models can make predictions almost instantaneously, making them extremely useful in real-time applications, design optimization, and iterative simulations.
   - Traditional Methods: Require significant computation time, particularly for complex structures like FG nanoplates and when piezoelectric effects are involved. The iterative nature of solving differential equations using FEM or other numerical methods adds to the computational cost.
4. Adaptability to New Configurations
   - AI: Can generalize from trained data, allowing it to predict the response of a wide range of nanoplate configurations, material distributions, and boundary conditions. AI models, especially deep learning, can adapt to new designs or variations with minimal reconfiguration.
   - Traditional Methods: Need to be recalculated from the ground up for each new configuration or parameter change, often requiring new formulations or mesh refinement.
5. Optimization and Inverse Problems
   - AI: Can solve optimization problems, such as maximizing energy harvesting from the piezoelectric patch, by learning from past simulations or datasets and guiding towards the optimal design. Techniques like genetic algorithm or particle swarm optimization can find the best combination of design parameters without exhaustive trial and error.
   - Traditional Methods: Require running numerous simulations with different parameter sets in a trial-and-error manner to achieve optimization, which can be slow and inefficient for complex systems.
6. Data-Driven Insights

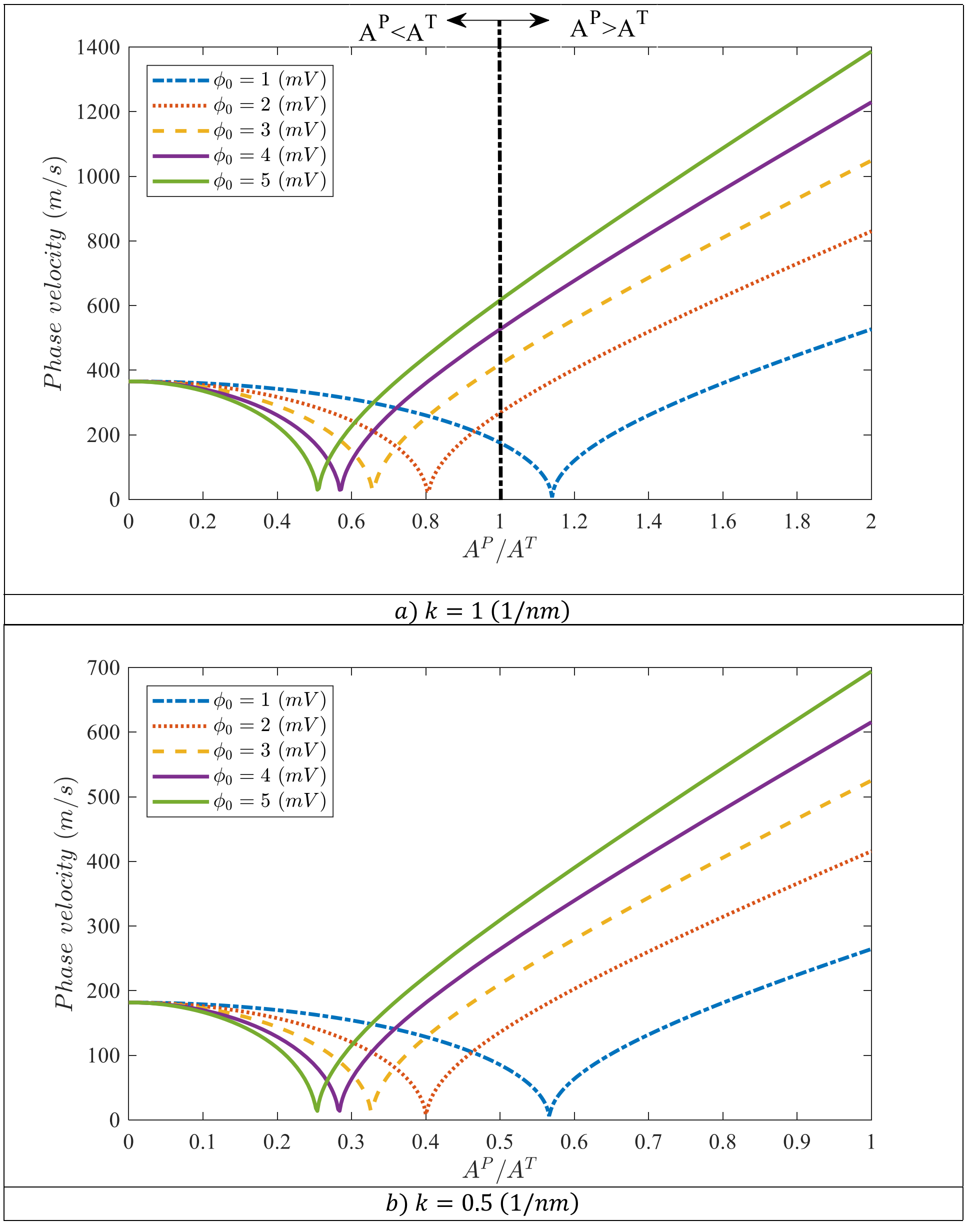

Fig. 6. Dependency of the phase velocity of the mentioned FG (ceramic-metal) structure on the ratio A^P/A^T for different values of applied voltages with $h = 0.1(nm)$, $b = a$, $a = 10h$, $l = \frac{h}{10}$, $\mu = \frac{h}{10}$, and n_x, n_y, $n_z = 0.5$.

- AI: Extracts insights and trends directly from data, revealing hidden patterns and correlations that may not be immediately evident through traditional theoretical or numerical methods. This can help engineers understand the sensitivity of different design parameters on vibrations and energy capacity.
- Traditional Methods: Focus on solving equations derived from physical laws, which might not expose all relevant trends, especially in multi-parameter systems like FG nanoplates coupled with piezoelectric patches.

7. Reduction in Modeling Errors
   - AI: Once trained with high-quality data, can reduce human error in modeling and simulations, as it relies on learning from accurate datasets and observed phenomena.
   - Traditional Methods: May introduce errors through incorrect assumptions, simplifications, or mesh discretization issues, especially when dealing with complex geometries or material gradients.
8. Cost-Effective
   - AI: Provides significant cost savings in terms of computational resources and time after the initial training phase. Once trained, models can predict the outcomes for a wide range of scenarios without needing new simulations or experiments.
   - Traditional Methods: Require expensive computational resources and high time investments for each new simulation, especially in high-fidelity models that require large meshes or intricate boundary conditions.

4.1. *Mathematics formulation of the mentioned AI algorithm*

o formulates the mathematics behind using AI for predicting the vibrations and energy capacity of a tri-directional functionally graded (FG) nanoplate attached to a piezoelectric patch, we must first understand how AI techniques (such as machine learning models) can be applied to this problem.

Here is a step-by-step breakdown of the mathematical formulation

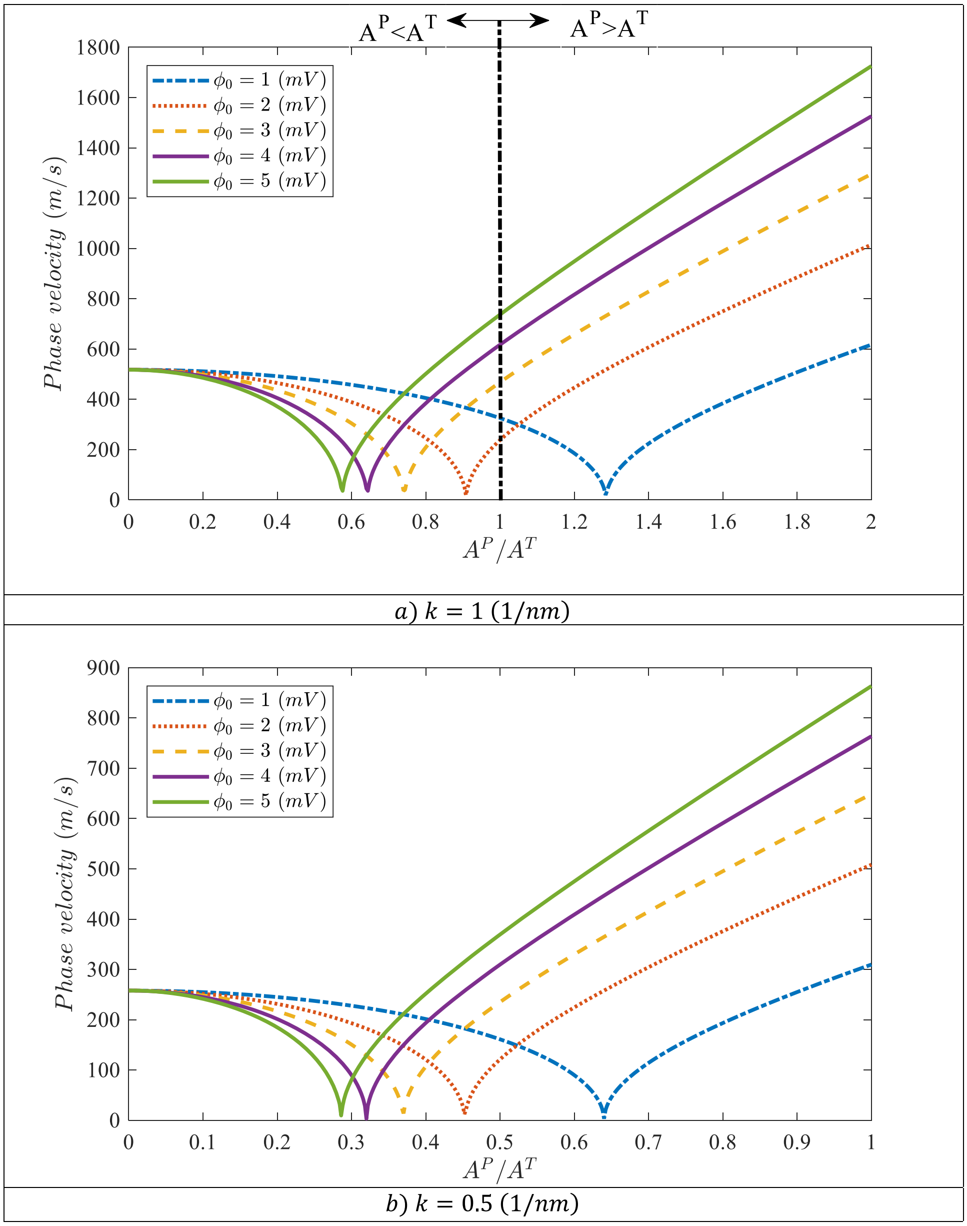

Fig. 7. Dependency of the phase velocity of the mentioned FG (metal-ceramic) structure on the ratio $A^{\mathscr{P}}/A^T$ for different values of applied voltages with $h = 0.1(nm)$, $b = a$, $a = 10h$, $l = \frac{h}{10}$, $\mu = \frac{h}{10}$, $k = 1\ (1/nm)$, and n_x, n_y, $n_z = 0.5$.

for using AI to predict the vibration characteristics and energy capacity:

1. Problem Representation

Let's define the problem using a dataset of input-output relationships derived from simulations or experiments.

- **Input Variables (Features):**
  - X_1: Material properties (Young's modulus, Poisson's ratio, density) as a function of thickness for the FG nanoplate.
  - X_2: Geometrical parameters (length, width, thickness).
  - X_3: Piezoelectric material properties (coupling coefficients, permittivity).
  - X_4: Boundary conditions.
  - X_5: External forces or vibrations applied to the nanoplate.
  - X_6: Temperature effects (if thermal conditions are considered).
- **Output Variables (Targets):**
  - Y_1: Natural frequencies ω\omegaω (e.g., linear and nonlinear frequencies).
  - Y_2: Vibration mode shapes.
  - Y_3: Energy capacity EEE harvested by the piezoelectric patch.

We define the system's input-output relationship in a general form:

$$Y = f(X) + \epsilon. \tag{29}$$

where $f(X)$ represents the underlying relationship between inputs X and outputs Y, and ϵ is the error term that accounts for uncertainties or noise.

2. Training Data Generation

Generate a dataset $\{X^{(i)}, Y^{(i)}\}_{i=1}^{N}$ where N is the number of data points obtained from:

- Finite element simulations.
- Analytical solutions (if available).
- Experimental measurements.

Each $X^{(i)}$ corresponds to a set of material, geometric, and loading parameters, and $Y^{(i)}$ corresponds to the resulting natural frequencies

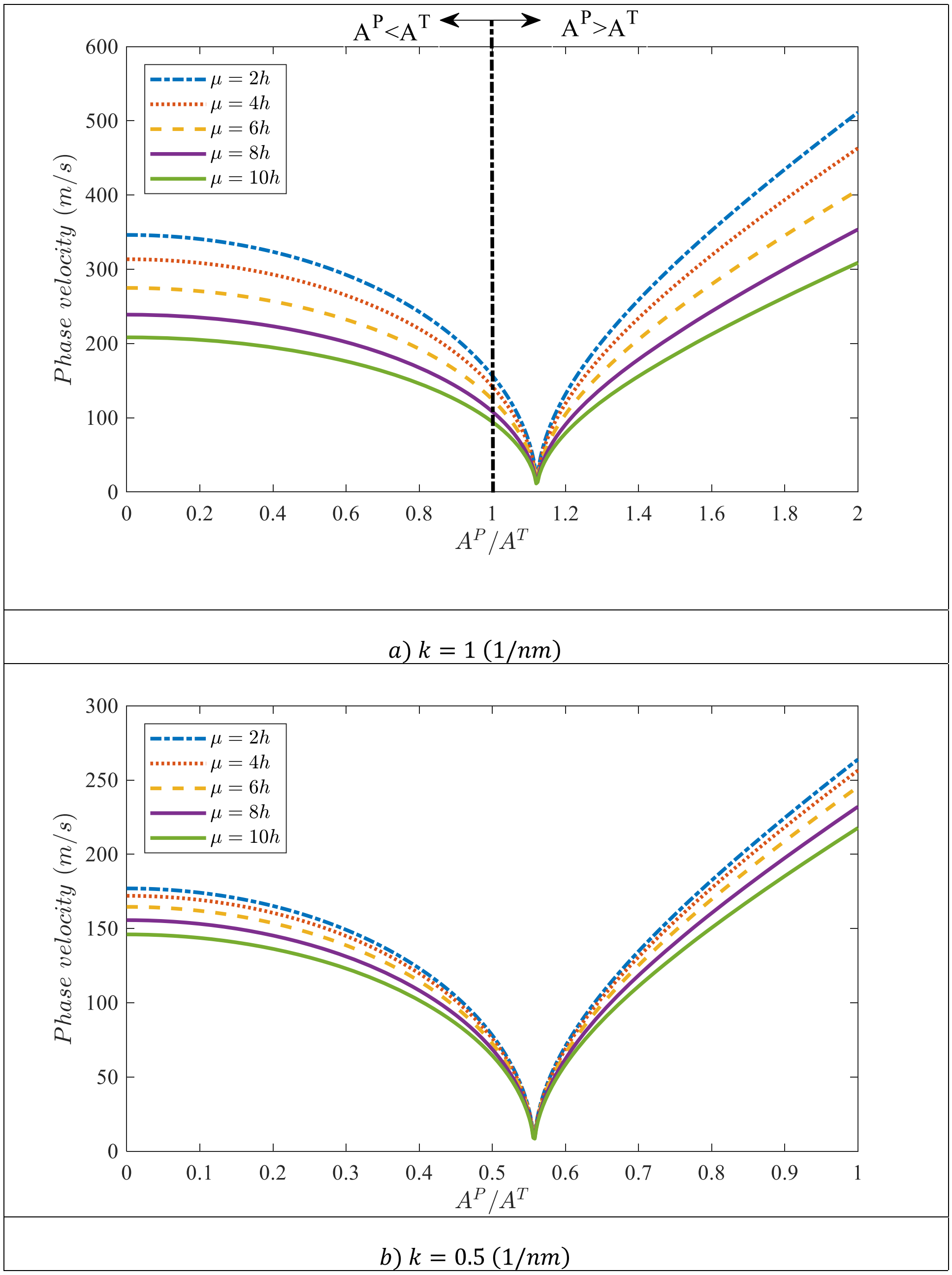

Fig. 8. Dependency of the phase velocity of the mentioned FG (ceramic-metal) structure on the ratio A^P/A^T for different values of nonlocal parameters for $h = 0.1(nm)$, $b = a$, $a = 10h$, $l = 0$, $k = 1\ (1/nm)$, ceramic/metal, n_x, n_y, $n_z = 0.5$, and $\varnothing_0 = 1\ (mV)$.

and energy capacity.

3. Artificial Intelligence Model

To predict the relationship between the input features and output targets, a machine learning model can be used. The most common AI approache is deep neural networks. For complex nonlinear problems like this, a neural network is a suitable model.

- **Neural Network Structure**: A feed-forward neural network with multiple layers (deep learning) can approximate any continuous function using the following formulation:
  - **Input Layer**: $X \in R^n$ (input features: material properties, geometry, etc.).
  - **Hidden Layers**: Nonlinear activation functions transform the input through a series of hidden layers:

$$z^{(l)} = W^{(l)}a^{(l-1)} + b^{(l)},\quad a^{(l)} = \sigma\left(z^{(l)}\right). \tag{30}$$

where $W^{(l)}$ and $b^{(l)}$ are the weight matrix and bias vector for the $l-th$ layer, $\sigma(\cdot)$ is the activation function (e.g., ReLU, sigmoid), and $a^{(l)}$ is the activation output from the layer.
  - **Output Layer**: The final output predicts the natural frequencies and energy capacity.

$$\widehat{Y} = W^{(L)}a^{(L-1)} + b^{(L)}. \tag{31}$$

- **Loss Function**: The model's performance is quantified using a loss function, typically the Mean Squared Error (MSE) for regression tasks:

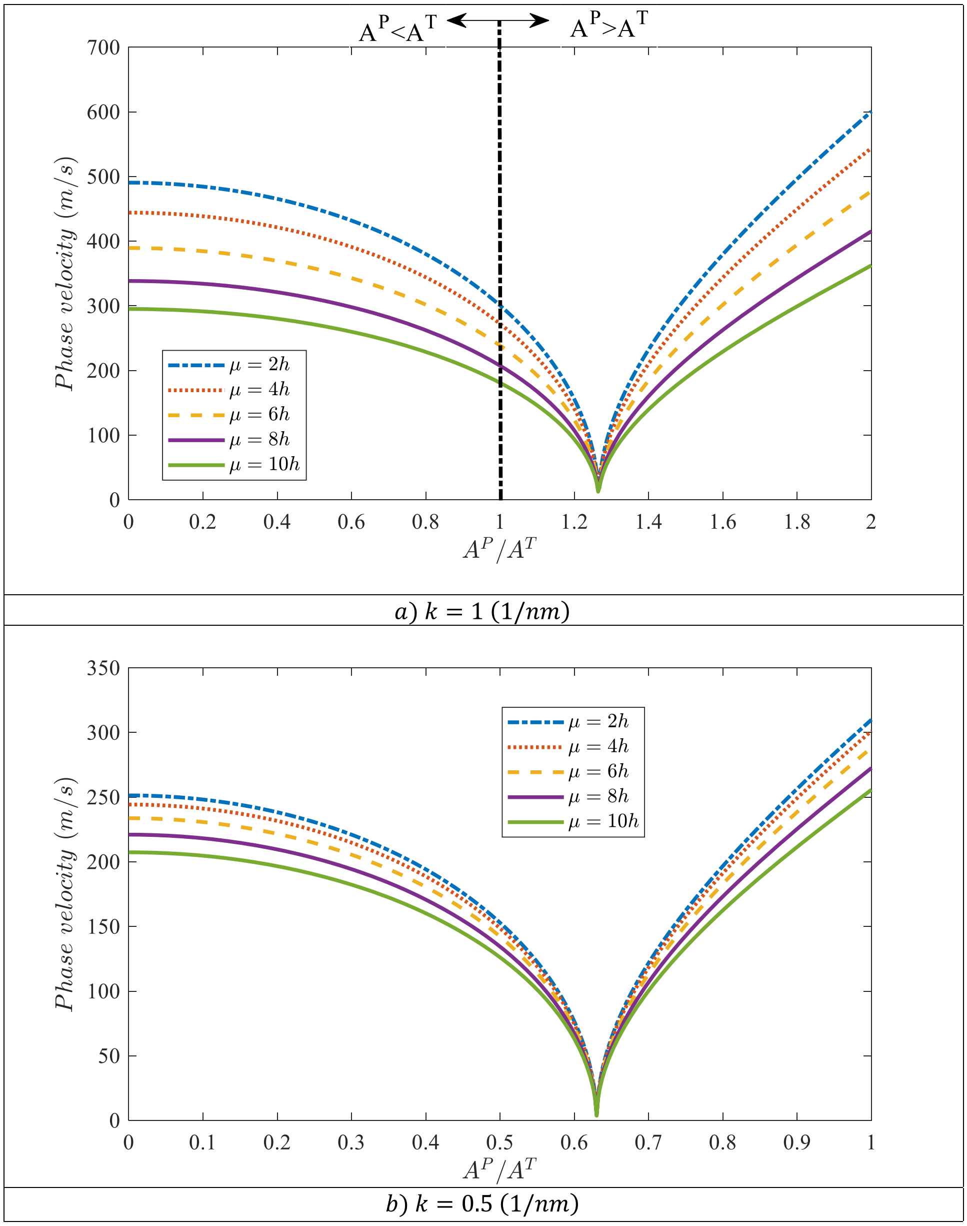

Fig. 9. Dependency of the phase velocity of the mentioned FG (metal-ceramic) structure on the ratio A^P/A^T for different values of nonlocal parameters and wave numbers for $h = 0.1(nm)$, $b = a$, $a = 10h$, $l = 0$, $k = 1$ $(1/nm)$, metal/ceramic, n_x, n_y, $n_z = 0.5$, and $\varnothing_0 = 1$ (mV).

$$L = (1/N) \sum_{i=1}^{N} \left(Y^{(i)} - \widehat{Y}^{(i)}\right)^2 \tag{32}$$

The neural network minimizes this loss by adjusting weights $W^{(L)}$ and biases $b^{(L)}$ using an optimization algorithm like gradient descent.

4. Optimization Algorithm for Parameter Tuning

Optimization algorithm can be employed to improve the accuracy and efficiency of predictions:

- Particle Swarm Optimization (PSO): PSO is used to optimize the hyperparameters of the neural network (e.g., learning rate, number of layers, number of neurons). The objective function to minimize is the validation loss L.

5. Model Validation

After training, the AI model is validated using unseen data from either:

- Experimental results.
- Simulation data not used during training.
- Analytical or benchmark solutions.

The prediction error is computed as:

$$Error = \frac{1}{M} \sum_{j=1}^{M} \left| Y_J^{true} - \widehat{Y}_j \right|. \tag{33}$$

where M is the number of validation data points, Y_J^{true} are the true values, and $\widehat{Y}_j$ are the AI model's predictions.

6. Final Model Output

Once trained and validated, the AI model can predict:

- Natural frequencies for new FG nanoplate configurations.

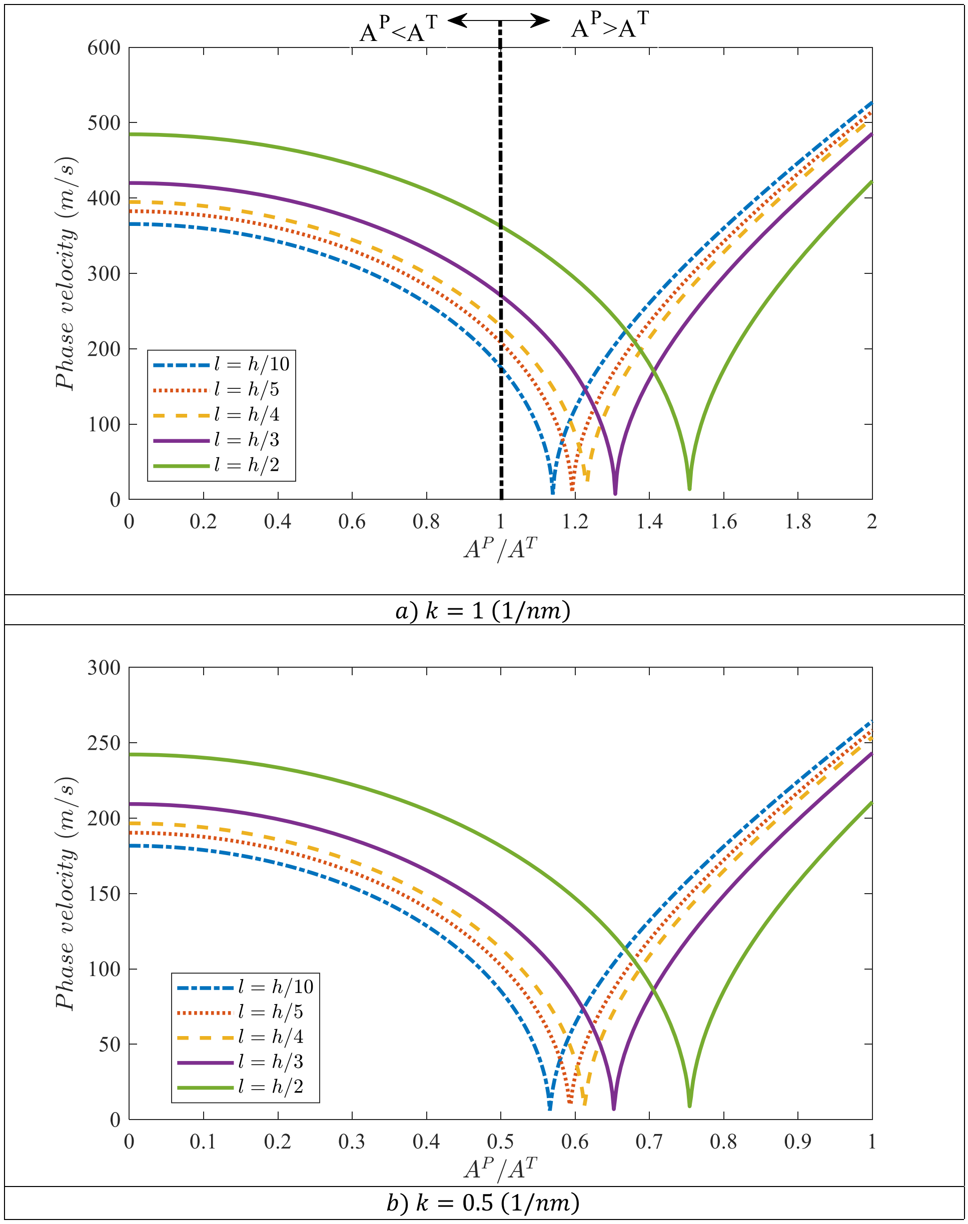

Fig. 10. Dependency of the phase velocity of the mentioned FG (ceramic-metal) structure on the ratio A^P/A^T for different values of length scale and wave numbers with $h = 0.1(nm)$, $b = a$, $a = 10h$, $\mu = 0$, $k = 1\ (1/nm)$, n_x, n_y, $n_z = 0.5$, and $\varnothing_0 = 1\ (mV)$.

- Energy harvesting capacity from the piezoelectric patch based on given inputs.

These predictions will be computationally efficient and can be used in real-time analysis or design optimization.

5. COMSOL multi-physics simulation

COMSOL Multiphysics is a powerful finite element simulation platform widely used to model and predict the behavior of complex physical systems, including sandwich nanoplates coupled with piezoelectric patches. In these systems, accurately predicting phase velocity is critical for assessing wave propagation characteristics, structural integrity, and energy efficiency in applications such as sensing, actuation, and vibration control. The sandwich nanoplate typically consists of a lightweight core material sandwiched between stiff face sheets, which provides enhanced stiffness-to-weight ratios, while the piezoelectric patch enables active control by converting mechanical strain into electrical energy and vice versa. The simulation in COMSOL begins by defining the geometry of the sandwich nanoplate and piezoelectric patch, followed by the specification of material properties, including mechanical and electrical characteristics. The coupling between the mechanical deformations of the nanoplate and the piezoelectric patch is handled through multi-physics interfaces, combining structural mechanics and electrostatics to simulate the interaction between electric fields and mechanical stresses. The non-homogeneous nature of the sandwich structure is incorporated through layered composite modeling, which accounts for different material properties across the thickness. To predict the phase velocity, harmonic wave analysis is performed, simulating wave propagation through the structure. The phase velocity depends on the stiffness, mass distribution, and piezoelectric coupling, all of which are influenced by the geometry and material properties. The quasi-3D deformation behavior of the sandwich nanoplate and the piezoelectric effects are captured by solving coupled partial differential equations using the finite element method. COMSOL's flexibility allows for the integration of advanced theories, such as nonlocal elasticity or shear

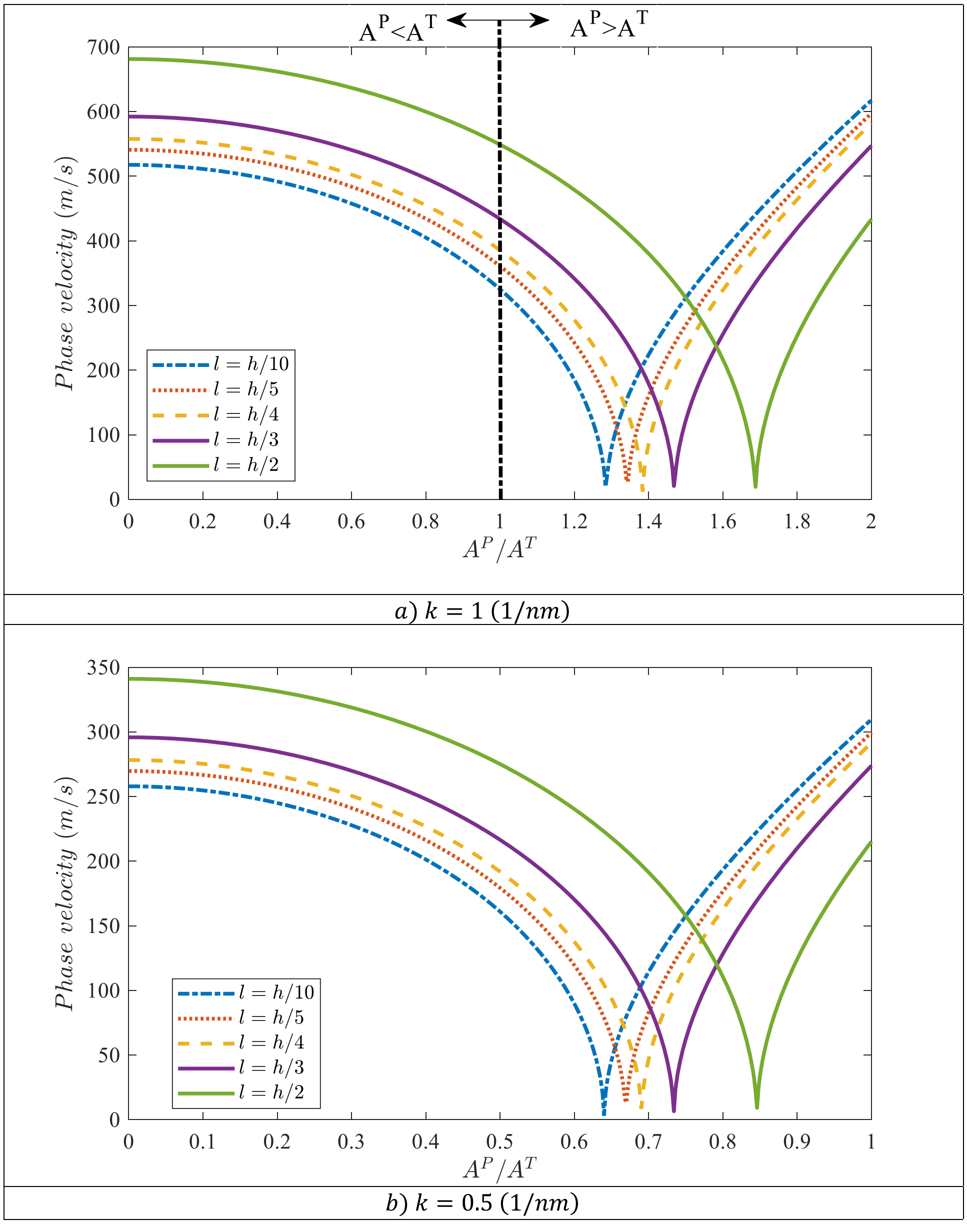

Fig. 11. Dependency of the phase velocity of the mentioned FG (metal-ceramic) structure on the ratio A^P/A^T for different values of length scale for $h = 0.1(nm)$, $b = a$, $a = 10h$, $\mu = 0$, $k = 1\ (1/nm)$, n_x, n_y, $n_z = 0.5$, and $\varnothing_0 = 1\ (mV)$.

deformation theories, to further enhance accuracy. The results offer insights into phase velocity and energy transmission, aiding in the design and optimization of piezoelectric-coupled sandwich structures for applications in nanotechnology, aerospace, and smart materials. In the simulation of phase velocity in a sandwich nanoplate coupled with a piezoelectric patch using COMSOL Multiphysics, a combination of tetrahedral mesh for the 3D geometry, quadrilateral mesh for thin layers, and boundary layer mesh near the interfaces is employed to ensure accurate representation of mechanical and electrical interactions.

6. Results and discussion

The effects of many factors, such as the location, nonlocal parameter, length scale factor, FG power index, and form of the piezoelectric patch, on the phase velocity, are discussed in detail in this section. Unless specified otherwise, the material properties given in Tables 1 and 2 have been used in analytical calculations for the nanoplates made of the FGM and PTZ-4 composites.

6.1. Verification study

Table 3 presents a comparison of circular frequencies (ω) for different mode numbers (k = 2, 5, 8, 11, 14, 17, 20, and 23) for a circular plate. The results are derived using the current study's method (labeled as "Present") and are compared with those from previous Refs. [47–49]. Each row in the table shows the natural frequencies (in radians per second) for a particular mode number, k, as calculated by the present method and compared to the results of Refs. [47–49]. The comparison demonstrates good agreement, especially for lower and intermediate mode numbers. Slight discrepancies can be observed at higher modes (e.g., $k = 23$), which could result from differences in numerical methods or boundary conditions. This validates the accuracy and reliability of the present approach in estimating natural frequencies in comparison to established methods from the literature.

Table 4 presents a comparison of the first dimensionless fundamental

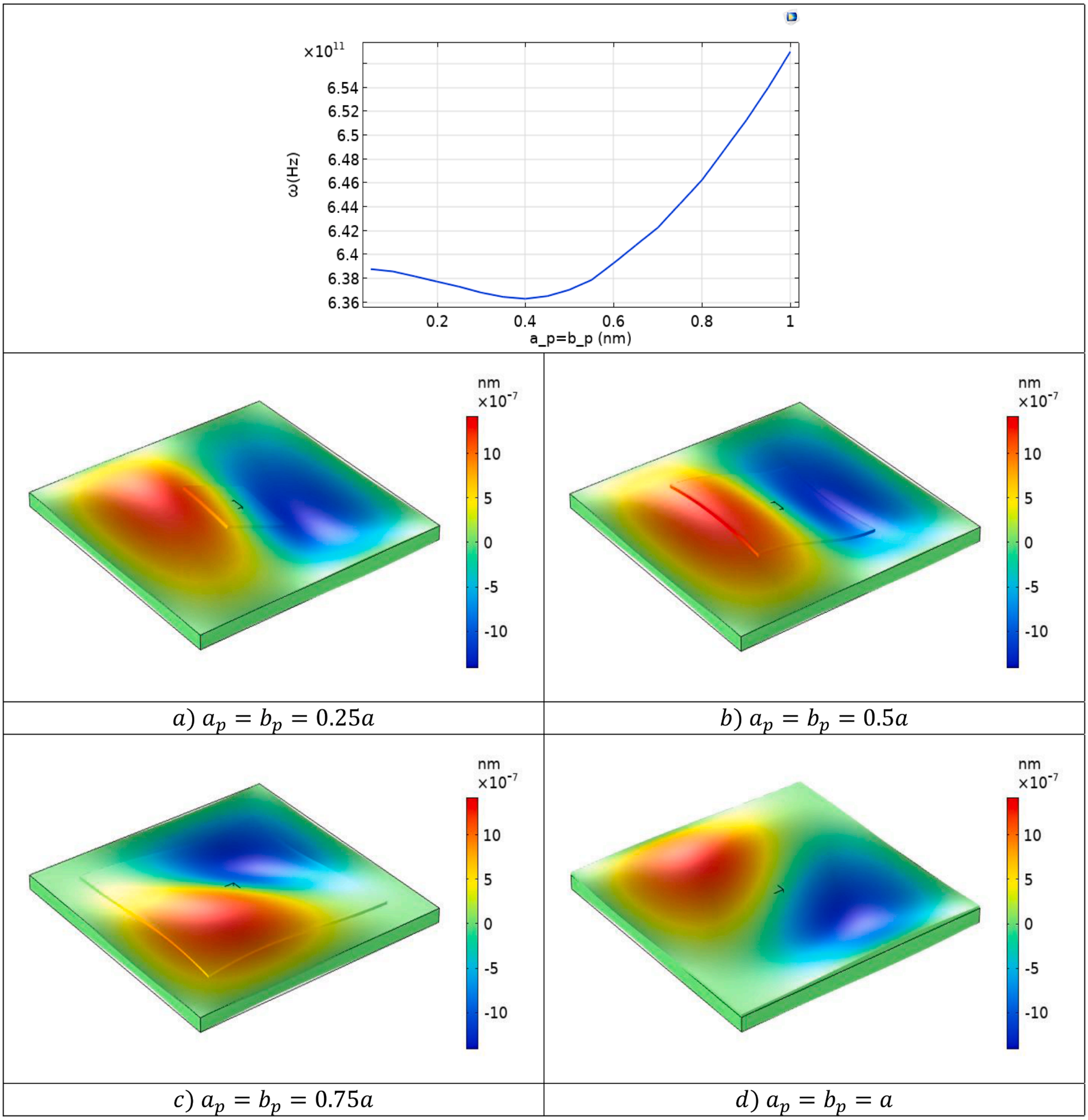

Fig. 12. The impact of the various length and width of piezoelectric layer on the maximum deflection of the sandwich rectangular plate for mode 3, $a = 1$ (nm), $b = a$, $h = \frac{a}{20}$, $h_p = \frac{h}{5}$, n_x, n_y, $n_z = 1$, and $\varnothing_0 = 1(mV)$.

frequencies of functionally graded nanoplates, focusing on how these frequencies vary with nonlocality, aspect ratio (a/b), and length-to-thickness ratio (a/h). Results from the present study are compared with those from Ref. [50]. For each aspect ratio ($a/b = 1$ and $a/b = 2$), and for different values of μ the dimensionless fundamental frequencies are tabulated. As the nonlocal parameter increases, the frequencies generally decrease, indicating a softening effect due to nonlocal elasticity. The influence of a/h is also evident, with lower frequencies observed for $a/h = 20$ compared to $a/h = 10$, highlighting the effect of increasing the plate's slenderness. The results show good agreement between the present study and Ref. [50], with only minor deviations, indicating that the method used in the present study accurately captures the dynamic behavior of functionally graded nanoplates. This comparison validates the reliability of the present model across varying geometric and nonlocal conditions.

6.2. Parametric results

In NEMS, the relationship between energy absorption capacity and phase velocity can be complex and is influenced by various factors. NEMS are devices that involve the interaction of mechanical and electrical phenomena at the nanoscale. The energy absorption capacity of a NEMS device refers to its ability to dissipate or absorb energy when subjected to mechanical or electrical inputs. This capacity can be

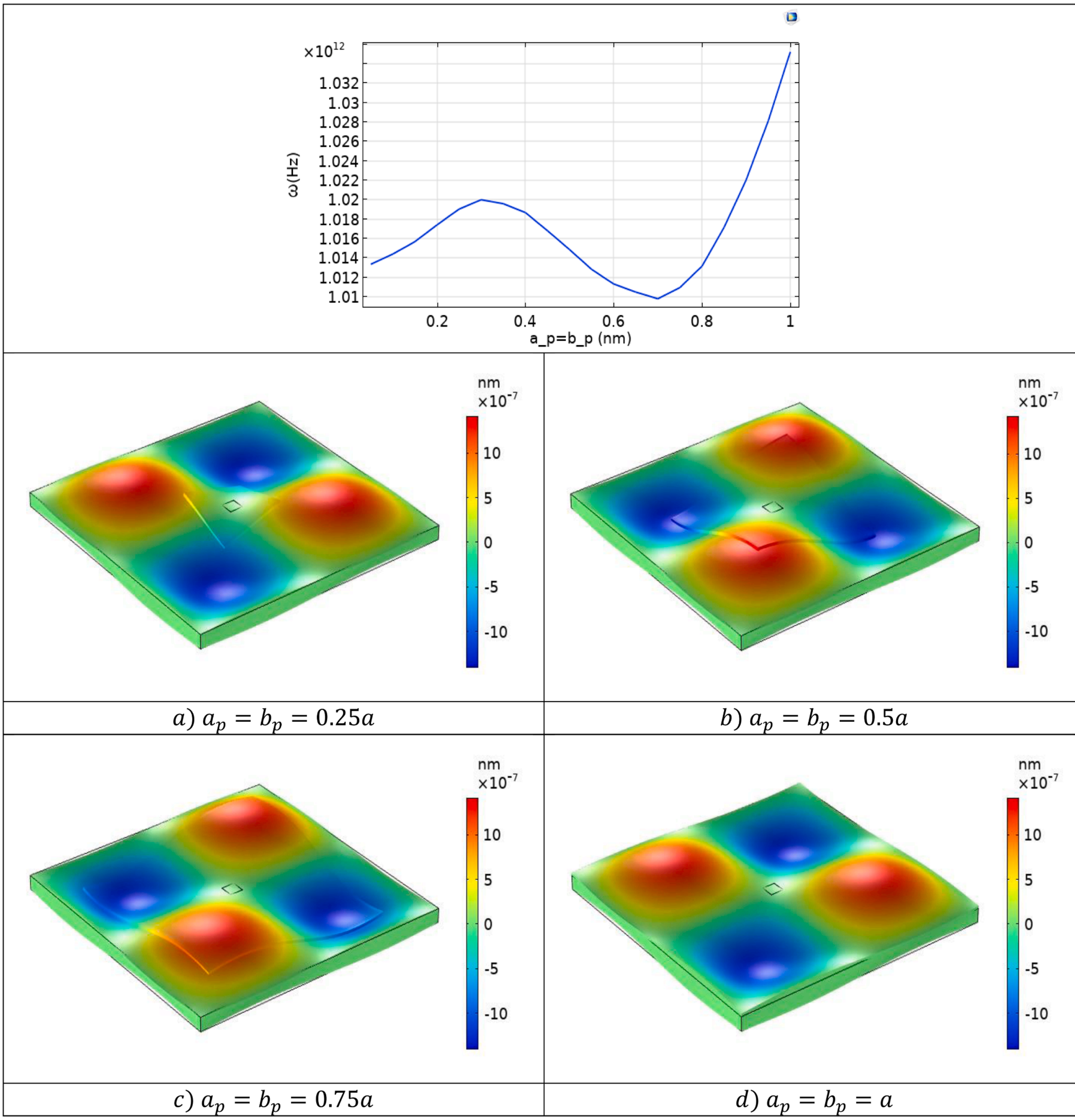

Fig. 13. The impact of the various length and width piezoelectric layers on the maximum deflection of the sandwich rectangular plate for mode 4, $a = 1$ (nm), $b = a$, $h = \frac{a}{20}$, $h_p = \frac{h}{5}$, n_x, n_y, $n_z = 1$, and $\varnothing_0 = 1(mV)$.

influenced by the material properties, structural design, and operating conditions of the NEMS device. The phase velocity in NEMS refers to the speed at which a wave or vibration propagates through the device. The phase velocity is influenced by the mechanical properties of the device, such as its mass, stiffness, and damping characteristics. The relationship between energy absorption capacity and phase velocity in NEMS can be understood through the concept of resonance. Resonance occurs when the frequency of an external force matches the natural frequency of the NEMS device, leading to a significant increase in energy absorption. In some cases, higher phase velocities in NEMS devices can lead to enhanced energy absorption capacity. This can occur when the higher phase velocity allows the device to efficiently dissipate energy through damping mechanisms or when it enables the device to interact more effectively with external stimuli. However, the relationship between energy absorption capacity and phase velocity can also be influenced by trade-offs. For example, increasing the phase velocity in a NEMS device may lead to reduced energy absorption capacity if it results in decreased damping or increased stiffness that limits the device's ability to dissipate energy. Overall, the relationship between energy absorption capacity and phase velocity in NEMS devices is a complex and multifaceted aspect of their behavior. So, it can be concluded that phase velocity and energy absorption have a direct influence on each other. Fig. 3 shows the influence of the A^P to A^T ratio of the structure on the energy absorption capacity of the presented composite structure. As is seen, by increasing

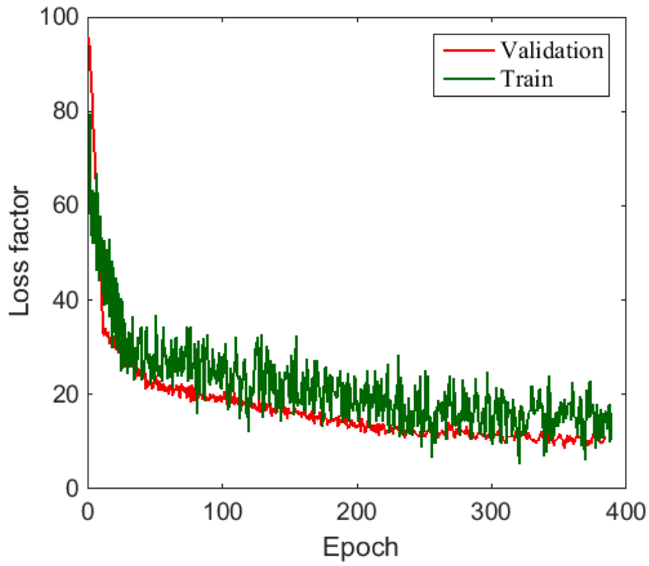

Fig. 14. Loss factor against epoch for the mentioned artificial intelligence algorithm

the A^P to A^T ratio the number of oscillations in a specific time decreases so, the stability and finally the absorbed energy in the system decreases.

In Fig. 4, it is demonstrated that with increasing the gradient index of the FG plate in all directions, the critical area ratio becomes less for a range of piezoelectric patch area to rectangular FG plate area ratio. In addition, prior to total values of area ratio, which is the value of interest in the application, the phase velocity decreases with an increase in the gradient indices. It is worth mentioning that the area of the piezoelectric patch is taken to be less than the plate area, $\frac{A^P}{A^T} \leq 1$. In Fig. 4a, the change of the phase velocity is depicted for the wavenumber $k = 1\ /nm$, and in Fig. 4b, it is shown for $k\ = 0.5/nm$. As can be recognized for the lower wavenumber, the area ratio falls into the $\frac{A^P}{A^T} \leq 1$. Thus, for lower wavenumbers, a limitation must be put on the area ratio of the piezoelectric while there is no limitation in larger wave numbers since the critical area ratio occurs in $\frac{A^P}{A^T} \geq 1$ for all gradient indices.

For the different k factors, in Fig. 5, it is demonstrated that with increasing the gradient index of the FG plate in all directions, the critical area ratio becomes less for a range of piezoelectric patch area to rectangular FG plate area ratio. In addition, prior to critical values of area ratio, which is the values of interest in the application, the phase velocity decreases with an increase in the gradient indices. It is worth mentioning that the area of the piezoelectric patch is taken to be less than the plate area, $\frac{A^P}{A^T} \leq 1$. In Fig. 5a, the change of the phase velocity is depicted for the wavenumber $k = 1/nm$, and in Fig. 4b it is shown for $k\ = 0.5\ /nm$. As can be recognized for the lower wavenumber, the area ratio falls into the $\frac{A^P}{A^T} \leq 1$. Thus, for lower wavenumbers, a limitation must be put on the area ratio of the piezoelectric while there is no limitation in larger wave numbers since the critical area ratio occurs in $\frac{A^P}{A^T} \geq 1$ for all gradient indices. By comparing Figs. 4, 5 it is shown that considering metal-ceramic in fabrication of the presented FG structure has higher stability and phase velocity value than ceramic-metal structure

The correlation of the phase velocity with applied voltage and area ratio A^P/A^T is shown in Figs. 6a and 6b for wave numbers $k = \frac{1.0}{nm}$ and $= \frac{0.5}{nm}$, respectively. It can be observed that the critical area ratio increases for the greater wave number. Furthermore, the overall responses of the phase velocity to the applied voltage are similar in both cases. As the area ratio increases, the effect of the applied voltage becomes more dominant. At values under $A^P/A^T \leq 0.1$ The effect of applied voltage can be neglected.

The correlation of the phase velocity with applied voltage and area ratio $A^{\mathscr{P}}/A^T$ is shown in Figs. 7a and 7b for wave numbers $k = \frac{1.0}{nm}$ and $= \frac{0.5}{nm}$, respectively. It can be observed that the critical area ratio increases for the greater wave number. Furthermore, the overall responses of the phase velocity to the applied voltage are similar in both cases. As the area ratio increases, the effect of the applied voltage becomes more dominant. At values under $A^{\mathscr{P}}/A^T \leq 0.1$ The effect of applied voltage can be neglected.

In Fig. 8 for different applied voltages, the dependency of the phase velocity on the nonlocal parameter and area ratio is presented. The nonlocal parameter change does not alter the critical area ratio. At the greater wave number, the critical area ratio falls in area ratios greater than 1. Thus, it is more desirable in design to have a greater wave number so that the piezoelectric patch area can be selected with no limitation. As the applied voltage changes the critical area ratio increases. In general, the phase velocity increases with an increase in nonlocal parameters for both applied voltages. The effect is more obvious in lower values of area ratios.

Fig. 9 displays the dependency of phase velocity on the A^P/A^T for a tri-directional functionally graded nanoplate attached to a piezoelectric patch. Two subfigures are presented, with the phase velocity plotted on the y-axis and the A^P/A^T on the x-axis. The analysis considers different values of nonlocal parameters, representing the material's nonlocality effects, and wave numbers. In subfigure (a), for $k\ = 1\ (1\ /nm)$, phase velocity increases as the A^P/A^T moves away from 1, either increasing or decreasing. The curves represent different nonlocal parameter values, ranging from $\mu = 2h$ to $\mu\ = 10h$, where the highest nonlocal parameter leads to the lowest phase velocity. The critical point where A^P/A^T indicates that the phase velocity is minimized and symmetrical around this point. In subfigure (b), for $k\ = 0.5\ (1\ /nm)$, the same trends are observed but with lower phase velocity values compared to (a), highlighting the influence of smaller wave numbers. The dependency of phase velocity on nonlocal parameters remains evident, as higher values of μ correspond to reduced phase velocities. The figure effectively demonstrates how phase velocity changes with the ratio of material properties and the influence of nonlocal parameters, emphasizing the sensitivity of wave propagation characteristics to both material and structural parameters in nanoplates attached to piezoelectric patches.

Fig. 10 illustrates the dependency of phase velocity on the A^P/A^T for a tri-directional functionally graded (FG) nanoplate attached to a piezoelectric patch, considering various length scales and wave numbers. The phase velocity is plotted against the A^P/A^T, with two subfigures showing the results for different wave numbers. In subfigure (a), the wave number is set at $k\ = 1\ (1\ /nm)$. The phase velocity decreases as A^P/A^T approaches 1, reaches a minimum around this value, and increases again as the ratio moves away from 1. The different curves represent varying length scales, ranging from $l = h/10$ to $l\ = h/2$. As the length scale increases, the phase velocity decreases, indicating a strong dependency on the length scale. In subfigure (b), the wave number is lower at $k\ = 0.5\ (1\ /nm)$, and the overall phase velocity is also lower compared to subfigure (a). The trends remain similar, with phase velocity minimizing around $A^P/A^T\ = 1$ and varying significantly with length scale. Larger length scales result in slower phase velocities across the entire range of A^P/A^T. This figure demonstrates the influence of both length scale and wave number on the dynamic response of nanoplates, particularly their phase velocity, in the presence of piezoelectric effects. It highlights the importance of these parameters in determining wave propagation characteristics in nanostructured materials.

The effect of the length scale on the critical area ratio is depicted in Fig. 11. With increasing the length scale the critical area ratio increases. Thus, this parameter can be regarded as a control parameter of the critical area ratio. The two wave numbers $k = \frac{1.0}{nm}$ and $k = \frac{0.5}{nm}$ also changes the phase velocity response of the FG plate. At the wave number $k = \frac{1.0}{nm}$ the critical area ratio becomes greater than 1 for all length scales. On the other hand, for the wavenumber $k = \frac{0.5}{nm}$, all the critical area ratio

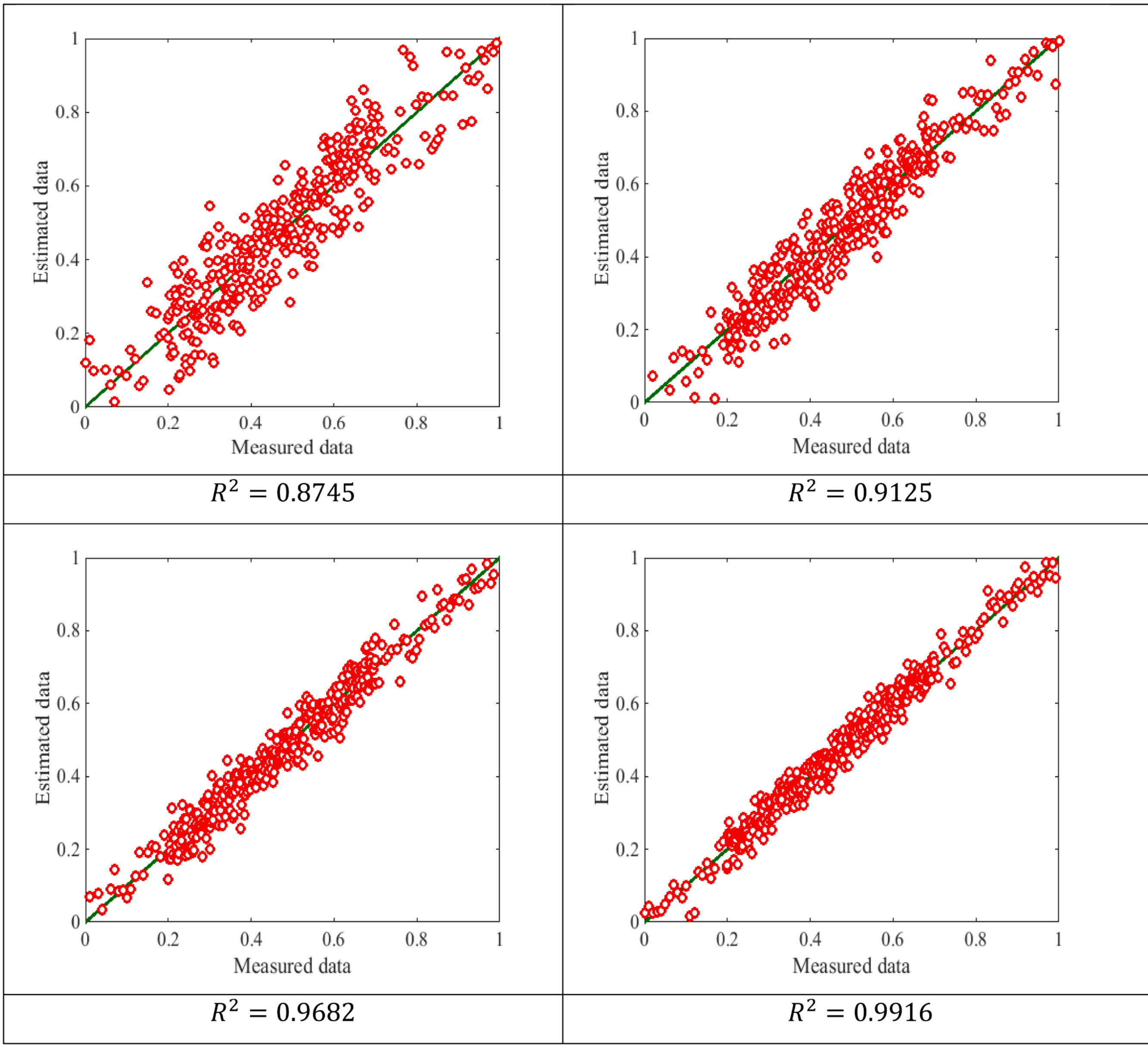

Fig. 15. Measured data against estimated data for various R^2 values of the mentioned artificial intelligence algorithm.

Table 5
Dimensionless frequency of the DNN model for different RMSE and h/l values

h/l	MSR	Predicted		
		$RMSE_{Train}=0.712$	$RMSE_{Train}=0.756$	$RMSE_{Train}=0.852$
10	175.521	142.172	10	175.521
5	182.932	148.1749	5	182.932
4	195.323	158.2116	4	195.323
3	203.355	164.7176	3	203.355
2	231.939	187.8706	2	231.939

Table 6
Performance of the DNN model for dimensionless frequency for various R^2 and μ/h

μ/h	MSR	Predicted		
		R^2=0.9352	R^2=0.9631	R^2=0.9916
2	205.921	181.8552	2	205.921
4	212.512	185.2598	4	212.512
6	223.931	193.6234	6	223.931
8	235.428	206.051	8	235.428
10	250.852	215.6986	10	250.852

values fall into the span less than unity. For a different boundary condition in Fig. 11a, similar behavior is observed. However, this change in boundary condition increases the critical area ratio in both wavenumbers. Generally, the phase velocity increases with an increase in length scale parameters.

The impact of the different lengths and widths of the piezoelectric layer on the maximum deflection and frequency of the rectangular sandwich plate for the first mode of frequency is shown in Fig. 12. It is clear that the size of the piezoelectric patch has a big impact on the NEMS frequency information. To put it another way, the frequency decreases as the size of the piezoelectric patch rises for low size values (a_p, b_p<0.4nm). However, for high size values (a_p, b_p >0.4 nm), an increase in the piezoelectric patch's size results in an increase in the NEMS frequency.

For the second mode of frequency, the effect of the piezoelectric patch's length and width on the amplitude and frequency of the NEMS coupled with the piezoelectric patch is presented in Fig. 13. As can be observed, the size of the piezoelectric patch has an important role in the frequency information and amplitude of the NEMS. For more detail, in the low values of size (a_p, b_p <0.3nm), by increasing the size of the piezoelectric patch, frequency increases. Also, in the high values of size (a_p, b_p >0.7nm) increase in the size of the piezoelectric patch results in an increase in the frequency of the NEMS. As an amazing result, in the middle value of the piezoelectric patch's size (0.3nm<a_p, b_p <0.7nm), an increase in the piezoelectric patch's size caused to increase in the frequency of the NEMS.

6.3. Deep neural networks to predict the mentioned problem

DNNs have emerged as a powerful tool for predicting complex physical phenomena such as the vibrations and energy capacity of tri-directional functionally graded nanoplates attached to piezoelectric patches. These systems exhibit intricate nonlinear behaviors due to their heterogeneous material properties and coupling effects between the nanoplate and the piezoelectric patch. Traditional analytical and numerical methods often require extensive computational resources and are limited by simplifying assumptions. DNNs offer a flexible, data-driven approach to model such systems by learning the underlying relationships from a dataset of simulations or experimental measurements. A DNN consists of multiple hidden layers, each containing several neurons, that progressively extract higher-level features from the input data. For this problem, the input features may include material properties (such as Young's modulus, Poisson's ratio), geometric parameters, and boundary conditions, while the outputs are the natural frequencies and energy harvesting capacities. By training the DNN using back-propagation and optimization techniques, the network adjusts its weights to minimize the error between predicted and actual values. The resulting model provides accurate predictions with reduced computational effort, making it an efficient alternative for real-time design optimization and dynamic analysis of advanced nanostructures. For training or tuning the AI model, optimization algorithm is used. Fig. 14 demonstrates the evolution of the loss factor over multiple epochs for both the training and validation datasets in an artificial intelligence algorithm. The rapid decrease in loss during the early epochs signifies effective initial learning, where the model quickly adjusts its weights to minimize prediction errors. The training loss, depicted by the green curve, exhibits significant fluctuations after the initial sharp decline, indicating the model continues fine-tuning its parameters. This oscillation is common in AI models during the training process, as the algorithm adjusts to variations in the dataset to improve performance. The validation loss, represented by the red curve, follows a similar trend but is notably smoother, implying that the model is generalizing well to unseen data without major fluctuations. The stabilization of both training and validation losses around lower values suggests that the model has reached convergence, achieving a balanced trade-off between bias and variance. The absence of a significant gap between training and validation loss curves indicates that overfitting is minimal, meaning the model's performance is consistent across both the training and validation sets. This trend highlights the robustness of the AI algorithm and its capacity to accurately predict outcomes while maintaining generalization across different datasets. The steady decline and eventual stabilization of the loss factor signify the effectiveness of the training process in optimizing the model's performance.

Fig. 15 displays four subplots, each showing a scatter plot of measured data against estimated data. The performance of an artificial intelligence algorithm is evaluated in terms of how well its estimated values correspond to the measured ones. In each plot, red circular markers represent the data points, and a green line is drawn to indicate perfect agreement between the estimated and measured data. The closer the points align to the green line, the better the accuracy of the model. Each subplot is annotated with a coefficient of determination (R^2) value, which quantifies the goodness-of-fit. The four subplots exhibit different R^2 values: 0.8745, 0.9125, 0.9682, and 0.9916. As the R^2 value increases, the scatter points show better alignment with the green line, indicating improved model performance. For instance, in the subplot with $R^2 = 0.9916$, almost all points closely follow the green line, reflecting a near-perfect estimation. In contrast, the subplot with $R^2 = 0.8745$ shows more scatter, suggesting lower predictive accuracy. In summary, these visual comparisons show that the AI algorithm's ability to predict the measured data improves with increasing R^2 values, reflecting its capacity for more accurate estimations as the correlation between measured and estimated data strengthens.

This section looks at how R^2 and RMSE affect the outcomes shown in Tables 5 and 6. Higher RMSE and R^2 values have been observed to result in more accurate replies. As a result, while choosing the results, it is advised to pick R^2=0.9916, RMSE=0.852, and 4120 samples. Mathematics simulation results (MSR) also present the outcomes of the mathematical modeling.

Tables 5 and 6 illustrate how the dimensionless frequency of the current structure varies with h/l and μ/h. This topic will be covered in more detail in the following section.

Here are some common parameter values used for this algorithm. After testing and training the datasets, the following results are obtained.

Particle Swarm Optimization:

- Population Size: 90 particles.
- Inertia Weight: 0.5.
- Cognitive Coefficient c_1 and Social Coefficient c_2: 1.4.
- Number of Iterations: 300.

Neural Network Parameters:

- Hidden layers: 5.
- Neurons per layer: 200.
- Activation functions: ReLU for hidden layers.
- Learning rate: 10^{-5}.
- Batch size: 128.
- Epochs: 300.
- R^2: 0. 9916
- RMSE: 0.852

7. Conclusion

Absorbed energy capacity, and wave propagation in NEMS hold significant importance in the aerospace industry due to their critical role in enhancing the performance, reliability, and safety of aerospace structures and systems. One key area of application is in the development of advanced sensors and actuators. NEMS-based sensors, utilizing wave propagation principles, can detect minute changes in environmental conditions, such as temperature, pressure, and stress, with high precision. This capability is essential for monitoring the structural health of aerospace components, ensuring early detection of potential issues, and preventing catastrophic failure. In the current work, dynamic stability analysis of the NEMS coupled with a piezoelectric patch was presented. For capturing the size effects, nonlocal strain-stress gradient theory with two size-dependent factors was presented. For modeling the displacement fields, a new four-variable refined quasi-3D logarithmic shear deformation theory was investigated. Also, for coupling the piezoelectric patch and composite structure, compatibility conditions were presented. Hamilton's principle with three factors was presented for obtaining the coupled governing equations of the NEMS. For solving the current electrical system's partial differential equations, an analytical solution procedure was presented. Also, to gain a better understanding of the current electrical system's fundamental frequency, a COMSOL multi-physics simulation was presented. For verification of the results, one of the tools of artificial intelligence via the datasets of the mathematics and COMSOL multi-physics simulations was presented to verify the results for other input data with low computational cost. In the results section, the effects of various factors such as the geometry of the piezoelectric patch, FG power index, length scale factor, nonlocal parameter, and location of piezoelectric patch on the phase velocity were discussed. Finally, some suggestions for improving the stability performance of the NEMS were presented in detail. The following points can be achieved from the results and discussion section:

✓ In the middle value of the piezoelectric patch's size (0.3nm$<a_p$, b_p $<$0.7nm), an increase in the piezoelectric patch's size caused to increase in the frequency of the NEMS.
✓ For high size values (a_p, b_p $>$0.4 nm), an increase in the piezoelectric patch's size results in an increase in the NEMS frequency.
✓ The dependency of phase velocity on nonlocal parameters remains evident, as higher values of μ correspond to reduced phase velocities.
✓ The phase velocity increases with an increase in nonlocal parameters for both applied voltages.
✓ Considering metal-ceramic in the fabrication of the presented FG structure has higher stability and phase velocity value than ceramic-metal structure.
✓ By increasing the A^P to A^T ratio the number of oscillations in a specific time decreases so, the stability and finally the absorbed energy in the system decreases.

CRediT authorship contribution statement

Wenqing Yang: Investigation, Resources, Software, Validation, Visualization, Writing – review & editing. **Lei Chang:** Writing – review & editing, Writing – original draft, Visualization, Validation, Supervision, Software, Resources, Investigation. **Khalid A. Alnowibet:** Resources, Software, Validation, Writing – review & editing. **Mohammed El-Meligy:** Investigation, Resources, Validation, Writing – review & editing.

Declaration of competing interest

The authors declare that they have no conflict of interest.

Acknowledgment

The authors extend their appreciation to King Saud University, Saudi Arabia for funding this work through Researchers Supporting Project number (RSP2024R305), King Saud University, Riyadh, Saudi Arabia.

Data availability

Data will be made available on request.

References

[1] V.T.T. Anh, N.D. Dat, P.D. Nguyen, N.D. Duc, A nonlocal higher-order shear deformation approach for nonline ar static analysis of magneto-electro-elastic sandwich Micro/Nano-plates with FG-CNT core in hygrothermal environment, Aerospace Science and Technology 147 (2024) 109069, https://doi.org/10.1016/j.ast.2024.109069, 2024/04/01/.
[2] M. Javani, M.R. Eslami, Y. Kiani, Active control of thermally induced vibrations of temperature-dependent FGM circular plate with piezoelectric sensor/actuator layers, Aerospace Science and Technology 146 (2024) 108997, https://doi.org/10.1016/j.ast.2024.108997, 2024/03/01/.
[3] I. Bruant, L. Proslier, Improved active control of a functionally graded material beam with piezoelectric patches, Journal of Vibration and Control 21 (10) (2013) 2059–2080, https://doi.org/10.1177/1077546313506926, 2015/07/01.
[4] J. Huo, G. Zhang, A. Ghabussi, M. Habibi, Bending analysis of FG-GPLRC axisymmetric circular/annular sector plates by considering elastic foundation and horizontal friction force using 3D-poroelasticity theory, Composite Structures (2021) 114438, https://doi.org/10.1016/j.compstruct.2021.114438.
[5] F. Ebrahimi, A. Dabbagh, Wave propagation analysis of embedded nanoplates based on a nonlocal strain gradient-based surface piezoelectricity theory, The European Physical Journal Plus 132 (11) (2017) 449, https://doi.org/10.1140/epjp/i2017-11694-2, 2017/11/02.
[6] P.H. Wan, M.S.H. Al-Furjan, R. Kolahchi, Nonlinear flutter response and reliability of supersonic smart hybrid nanocomposite rupture trapezoidal plates subjected to yawed flow using DQHFEM, Aerospace Science and Technology 145 (2024) 108862, 2024.
[7] H. Safarpour, S.Ali Ghanizadeh, M. Habibi, Wave propagation characteristics of a cylindrical laminated composite nanoshell in thermal environment based on the nonlocal strain gradient theory, Eur. Phys. J. Plus 133 (12) (2018) 532, https://doi.org/10.1140/epjp/i2018-12385-2 [Online]. Available:.
[8] F. Ebrahimi, A. Dabbagh, Viscoelastic wave propagation analysis of axially motivated double-layered graphene sheets via nonlocal strain gradient theory, Waves in Random and Complex Media 30 (1) (2020) 157–176.
[9] X. Li, L. Li, Y. Hu, Z. Ding, W. Deng, Bending, buckling and vibration of axially functionally graded beams based on nonlocal strain gradient theory, Composite Structures 165 (2017) 250–265, https://doi.org/10.1016/j.compstruct.2017.01.032, 2017/04/01/.
[10] C. Dangi, R. Lal, N. Sukavanam, Effect of surface stresses on the dynamic behavior of bi-directional functionally graded nonlocal strain gradient nanobeams via generalized differential quadrature rule, European Journal of Mechanics - A/Solids 90 (2021) 104376, https://doi.org/10.1016/j.euromechsol.2021.104376, 2021/11/01/.
[11] M. Emadi, Z. Nejad Mohammad, S. Ziaee, A. Hadi, Buckling analysis of arbitrary two-directional functionally graded nano-plate based on nonlocal elasticity theory using generalized differential quadrature method (in En), Steel and Composite Structures 39 (5) (2021) 565–581, https://doi.org/10.12989/SCS.2021.39.5.565. /.
[12] J.P. Shen, P.Y. Wang, W.T. Gan, C. Li, Stability of Vibrating Functionally Graded Nanoplates with Axial Motion Based on the Nonlocal Strain Gradient Theory, International Journal of Structural Stability and Dynamics 20 (08) (2020) 2050088, https://doi.org/10.1142/s0219455420500881.
[13] M. Mahinzare, M. Jannat Alipour, S.A. Sadatsakkak, M. Ghadiri, A nonlocal strain gradient theory for dynamic modeling of a rotary thermo piezo electrically actuated nano FG circular plate, Mechanical Systems and Signal Processing 115 (2019) 323–337, https://doi.org/10.1016/j.ymssp.2018.05.043, 2019/01/15/.
[14] M.H. Kargarnovin, M.M. Najafizadeh, N.S. Viliani, Vibration control of a functionally graded material plate patched with piezoelectric actuators and sensors under a constant electric charge, Smart Materials and Structures 16 (4) (2007) 1252–1259, https://doi.org/10.1088/0964-1726/16/4/037, 2007/07/03.
[15] I. Bruant, L. Proslier, Optimal location of piezoelectric actuators for active vibration control of thin axially functionally graded beams, International Journal of Mechanics and Materials in Design 12 (2) (2016) 173–192, https://doi.org/10.1007/s10999-015-9297-y, 2016/06/01.
[16] P.L. Motlagh, M.R. Anamagh, B. Bediz, I. Basdogan, Electromechanical analysis of functionally graded panels with surface-integrated piezo-patches for optimal energy harvesting, Composite Structures 263 (2021) 113714, https://doi.org/10.1016/j.compstruct.2021.113714, 2021/05/01/.
[17] P.L. Motlagh, B. Bediz, I. Basdogan, A spectral Tchebychev solution for electromechanical analysis of thin curved panels with multiple integrated piezo-patches, JOURNAL OF SOUND AND VIBRATION 486 (2020) 115612.
[18] Q.-H. Pham, T.T. Tran, P.-C. Nguyen, Uncertain vibration characteristics of Bi-directional functionally graded sandwich nanoplate subjected to dynamic load, Thin-Walled Structures 193 (2023) 111206.
[19] T. Yıldız, I. Esen, The effect of the foam structure on the thermomechanical vibration response of smart sandwich nanoplates, Mechanics of Advanced Materials and Structures (2023) 1–19.
[20] F. Pehlivan, I. Esen, K.G. Aktas, The effect of the foam structure and distribution on the thermomechanical vibration behavior of sandwich nanoplates with magneto-electro-elastic face layers. Mechanics of Advanced Materials and Structures, 2024, pp. 1–30.
[21] C. Chu, L. Shan, M.S.H. Al-Furjan, A. Farrokhian, R. Kolahchi, Energy absorption, free and forced vibrations of flexoelectric nanocomposite magnetostrictive sandwich nanoplates with single sinusoidal edge on the frictional torsional viscoelastic medium, Archives of Civil and Mechanical Engineering 23 (4) (2023) 223, 2023.
[22] S. Rai, A. Gupta, Dynamic response of sandwich functionally graded nanoplate under thermal environments and elastic foundations using dynamic stiffness method, Scientific reports 14 (1) (2024) 21689.
[23] A. Alibeigloo, R. Madoliat, Static analysis of cross-ply laminated plates with integrated surface piezoelectric layers using differential quadrature, Composite Structures 88 (3) (2009) 342–353.
[24] A. Alibeigloo, Thermo-elasticity solution of functionally graded plates integrated with piezoelectric sensor and actuator layers, Journal of Thermal Stresses 33 (8) (2010) 754–774.
[25] A. Alibeigloo, Three-dimensional exact solution for functionally graded rectangular plate with integrated surface piezoelectric layers resting on elastic foundation, Mechanics of Advanced Materials and Structures 17 (3) (2010) 183–195.
[26] N. Namazinia, A. Alibeigloo, M. Karimiasl, Free vibration and static analysis of sandwich composite plate with auxetic core and GPLRC facing sheets in hygrothermal environment, Forces in Mechanics (2024) 100264, 2024.
[27] M. Jalaei, H. Thai, Ö. Civalek, On viscoelastic transient response of magnetically imperfect functionally graded nanobeams, International Journal of Engineering Science 172 (2022) 103629.
[28] M.H. Ghazwani, A. Alnujaie, M. Avcar, P. Van Vinh, Examination of the high-frequency behavior of functionally graded porous nanobeams using nonlocal simple higher-order shear deformation theory, Acta Mechanica (2024) 1–20.

[29] M. Avcar, L. Hadji, O. Civalek, The influence of non-linear carbon nanotube reinforcement on the natural frequencies of composite beams, Advances in Nano Research 14 (5) (2023) 421–433.

[30] L. Hadji, M. Avcar, and Ö. Civalek, "Free vibration of carbon nanotube–reinforced composite beams under the various boundary conditions," in *Advanced Composite Materials and Structures*: CRC Press, 2022, pp. 87-108.

[31] L. Hadji, M. Avcar, Nonlocal free vibration analysis of porous FG nanobeams using hyperbolic shear deformation beam theory, Advances in Nano Research 10 (3) (2021) 281–293.

[32] Ö. Civalek, M. Akpınar, B. Uzun, M.Ö. Yaylı, Dynamics of a non-circular-shaped nanorod with deformable boundaries based on second-order strain gradient theory, Archive of Applied Mechanics (2024) 1–18.

[33] R. Barretta, L. Feo, R. Luciano, F.M. de Sciarra, R. Penna, Functionally graded Timoshenko nanobeams: a novel nonlocal gradient formulation, Composites Part B: Engineering 100 (2016) 208–219.

[34] C. Lim, G. Zhang, J. Reddy, A higher-order nonlocal elasticity and strain gradient theory and its applications in wave propagation, Journal of the Mechanics and Physics of Solids 78 (2015) 298–313.

[35] E. C. Aifantis, "Strain gradient interpretation of size effects," in *Fracture scaling*: Springer, 1999, pp. 299-314.

[36] A.C. Eringen, J. Wegner, Nonlocal continuum field theories, Appl. Mech. Rev. 56 (2) (2003) B20–B22.

[37] T.-V. Vu, H.T.T. Nguyen, H. Nguyen-Van, T.-P. Nguyen, J.L. Curiel-Sosa, A refined quasi-3D logarithmic shear deformation theory-based effective meshfree method for analysis of functionally graded plates resting on the elastic foundation, Engineering Analysis with Boundary Elements 131 (2021) 174–193, https://doi.org/10.1016/j.enganabound.2021.06.021, 2021/10/01/.

[38] T. Fu, X. Wang, T. Rabczuk, Broadband low-frequency sound insulation of stiffened sandwich PFGM doubly-curved shells with positive, negative and zero Poisson's ratio cellular cores, Aerospace Science and Technology 147 (2024) 109049, https://doi.org/10.1016/j.ast.2024.109049, 2024/04/01/.

[39] K.-J. Sohn, J.-H. Kim, Nonlinear thermal flutter of functionally graded panels under a supersonic flow, Composite Structures 88 (3) (2009) 380–387.

[40] R. Aboutalebi, Three-dimensional flutter analysis of a novel circular sandwich plate employing hyperbolic shear deformation theory, Aerospace Science and Technology 150 (2024) 109223, https://doi.org/10.1016/j.ast.2024.109223, 2024/07/01/.

[41] R. Moradi-Dastjerdi, K. Behdinan, Stress waves in a lightweight substrate plate actuated with piezoelectric layers under sinusoidal time-dependent pressures, Aerospace Science and Technology 132 (2023) 108057, https://doi.org/10.1016/j.ast.2022.108057, 2023/01/01/.

[42] Y. Chai, Z. Song, F. Li, Investigations on the aerothermoelastic properties of composite laminated cylindrical shells with elastic boundaries in supersonic airflow based on the Rayleigh–Ritz method, Aerospace Science and Technology 82-83 (2018) 534–544, https://doi.org/10.1016/j.ast.2018.09.040, 2018/11/01/.

[43] Y. Qiu, J. Wang, A Machine Learning Approach to Credit Card Customer Segmentation for Economic Stability. ICEMBDA 2023: Proceedings of the 4th International Conference on Economic Management and Big Data Applications, ICEMBDA 2023, October 27–29, 2023, Tianjin, China, 2024.

[44] Y. Qiu. Estimation of tail risk measures in finance: Approaches to extreme value mixture modeling, Johns Hopkins University, 2019.

[45] J. Reddy, C. Chin, Thermomechanical analysis of functionally graded cylinders and plates, Journal of thermal Stresses 21 (6) (1998) 593–626.

[46] M. Pietrzakowski, Piezoelectric control of composite plate vibration: Effect of electric potential distribution, Computers & Structures 86 (9) (2008) 948–954.

[47] H. Aminipour, M. Janghorban, Wave propagation in anisotropic plates using trigonometric shear deformation theory, Mechanics of Advanced Materials and Structures 24 (13) (2017) 1135–1144.

[48] M.R. Nami, M. Janghorban, Wave propagation in rectangular nanoplates based on strain gradient theory with one gradient parameter with considering initial stress, Modern Physics Letters B 28 (03) (2014) 1450021.

[49] S.I. Tahir, A. Tounsi, A. Chikh, M.A. Al-Osta, S.U. Al-Dulaijan, M.M. Al-Zahrani, An integral four-variable hyperbolic HSDT for the wave propagation investigation of a ceramic-metal FGM plate with various porosity distributions resting on a viscoelastic foundation, Waves in Random and Complex Media 34 (3) (2024) 1616–1639.

[50] S. Natarajan, S. Chakraborty, M. Thangavel, S. Bordas, T. Rabczuk, Size-dependent free flexural vibration behavior of functionally graded nanoplates, Computational Materials Science 65 (2012) 74–80.